A dataset of microphysical cloud parameters, retrieved from Emission-FTIR spectra measured in Arctic summer 2017

Philipp Richter[1], Mathias Palm[1], Christine Weinzierl[1], Hannes Griesche[2], Penny M. Rowe[3], and Justus Notholt[1]

[1]University of Bremen, Institute of Environmental Physics, Otto-Hahn-Allee 1, 28359 Bremen
[2]Leibniz Institute for Tropospheric Research (TROPOS), Permoserstr. 15, 04318 Leipzig
[3]NorthWest Research Associates, Redmond, WA, USA

Correspondence: Philipp Richter (phi.richter@uni-bremen.de)

Abstract. A dataset of microphysical cloud parameters from optically thin clouds, retrieved from infrared spectral radiances measured in summer 2017 in the Arctic, is presented. Measurements were performed using a mobile Fourier-transform infrared (FTIR) spectrometer which was carried by the RV *Polarstern*. ~~This~~ The dataset contains retrieved optical depths and effective radii of ice and water, from which the liquid water path and ice water path are calculated. ~~These~~ The water paths and the

5 effective radii retrieved from the FTIR measurements are compared with derived quantities from a combined cloud radar, lidar and microwave radiometer measurement synergy retrieval, called Cloudnet. ~~Comparing~~ The purpose of this comparison is to benchmark the infrared retrieval data against the established Cloudnet retrieval. For the liquid water ~~paths from the infrared retrieval and Cloudnet shows significant correlations with a standard deviation of $8.20\,\mathrm{g\cdot m^{-2}}$~~ path, the data correlate, showing a mean bias of $2.48\,\mathrm{g\cdot m^{-2}}$ and a root-mean-square error of $10.43\,\mathrm{g\cdot m^{-2}}$. It follows that the infrared retrieval is able to

10 determine the liquid water path. Although liquid water path retrievals from ~~microwave radiometer~~ in the Cloudnet retrieval data come with ~~a~~ an uncertainty of at least $20\,\mathrm{g\cdot m^{-2}}$, a ~~significant correlation and a standard deviation of $5.32\,\mathrm{g\cdot m^{-2}}$ between the results of~~ root-mean-square error of $9.48\,\mathrm{g\cdot m^{-2}}$ for clouds with a ~~precipitable water vapour of less than $1\,\mathrm{cm}$ and a~~ liquid water path of at most $20\,\mathrm{g\cdot m^{-2}}$ ~~retrieved from infrared spectra and results from Cloudnet can be seen. Therefore the comparison with data retrieved from infrared spectra shows that optically~~ is found. This indicates that the liquid water paths especially

15 of thin clouds of the ~~measurement campaign in summer 2017 can be observed well using microwave radiometers within the Cloudnet framework~~ Cloudnet retrieval can be determined with higher accuracy than expected. Apart from this, the dataset of microphysical cloud properties presented here ~~allows~~ allow researchers to perform calculations of the cloud radiative effects, when the Cloudnet data from the campaign are not available, which was the case from the 22nd July 2017 until the 19th August 2017. The dataset is published at Pangaea (Richter et al., 2021).

1

1 Introduction

Clouds play an important role in the radiation budget of the earth. In the visible regime, clouds mainly reflect and prevent solar radiation from reaching earth's surface, whereas in the thermal regime clouds prevent surface radiation from escaping to space and re-emit it back to earth, where it warms the surface. In the Arctic, about 80% of the liquid water containing clouds have a liquid water path (LWP) below $100\,\mathrm{g\cdot m^{-2}}$ (Shupe and Intrieri, 2004), therefore observation of clouds bearing low amounts of liquid water is crucial to understand the effect of clouds on atmospheric radiation in the Arctic. The change of the broadband surface longwave radiative flux is largest up to a visible optical depth between 6 to 10 corresponding to a LWP of approximately $40\,\mathrm{g\cdot m^{-2}}$, depending on the effective droplet radius (Turner et al., 2007).

The observed warming in the Arctic is much greater than the warming of the rest of the Earth (Wendisch et al., 2019). This phenomenon is called Arctic Amplification. A large number of processes are known to influence the Arctic amplification, but the quantification of each process and its importance is difficult. The project Arctic Amplification: Climate Relevant Atmospheric and Surface Processes and Feedback Mechanisms $(\mathcal{AC})^3$ (Wendisch et al., 2019) aims to close this gap of knowledge by performing various campaigns, model studies and enduring measurements in the Arctic. The measurement campaign and the data presented in this paper are part of $(\mathcal{AC})^3$.

Usually microwave radiometers (MWR) are used for ground-based observations of liquid water clouds. MWR can detect liquid water paths above $100\,\mathrm{g\cdot m^{-2}}$, also they have the ability to operate continiously 24 hours a day, but LWP retrievals from MWR measurements suffer a high uncertainty in the LWP of at least $15\,\mathrm{g\cdot m^{-2}}$ (Löhnert and Crewell, 2003). For more accurate observations of optically thin clouds, Fourier Transform Infrared (FTIR) spectrometers can be used. Calibrated FTIR spectrometer are used for the observation of trace gases in absence of the sun or the moon as light source, done for example by Becker et al. (1999) and Becker and Notholt (2000), as well as for the observation of optically thin clouds, performed within the scope of the network Atmospheric Radiation Measurement (ARM) using Atmospheric Emitted Radiance Interferometer (AERI) (Knuteson et al. (2004a) and Knuteson et al. (2004b)). Although the sensitivity of the FTIR retrieval decreases from approximately $50\,\mathrm{g\cdot m^{-2}}$ (Turner et al., 2007), they can be used to supplement existing cloud observation techniques. In addition, an FTIR spectrometer can be used to determine the effective radii of the cloud droplets and the phase of a cloud. An emission FTIR spectrometer has been set up on the German research vessel *Polarstern* to perform measurements in summer 2017 in the Arctic around Svalbard.

Lacking freely available physical retrieval algorithms at the time of the measurement campaign, we decided to retrieve microphysical cloud parameters from spectral radiances using the retrieval algorithm Total Cloud Water retrieval (TCWret). TCWret uses the radiative transfer model LBLDIS (Turner, 2005), which includes LBLRTM (Clough et al., 2005) and DIS-

Table 1. Number of radiance measurements per cruise leg. Only measurements for which there is a successful retrieval are considered.

Crusie leg	Days with measurement	Measurements
PS106.1	9	1746
PS106.2	17	1915
PS107	15	1903

55 ORT (Stamnes et al., 1988). TCWret works on the spectral radiances from $558.5\,\mathrm{cm}^{-1}$ to $1163.4\,\mathrm{cm}^{-1}$, which are taken from (Turner, 2005) and adapted to the present instrumental setup. TCWret uses spectral windows where low absorption of gases occur and therefore the atmosphere is transparent for emissions from clouds. It uses an optimal estimation approach (Rodgers, 2000) and retrieves the liquid water optical depth τ_{liq}, the ice water optical depth τ_{ice} and their respective effective radii r_{liq} and r_{ice}. From this, the LWP and Ice Water Path (IWP) are calculated. The principle of this retrieval technique has been proven

60 already for mixed-phase clouds by the Mixed-phase cloud property retrieval algorithm (MIXCRA) by Turner (2005) and ~~later~~ by the CLoud and Atmospheric Radiation Retrieval Algorithm (CLARRA) by Rowe et al. (2019) and for single-phase liquid clouds using the thermal infrared spectral range (extended line-by-line atmospheric transmittance and radiance algorithm (XTRA) by Rathke and Fischer (2000)).

Section ~~2~~ 2 describes the measurement area ~~. In section 3 we give~~ and gives an overview of the measurement setup and proce-

65 dure. In section ~~4~~3, the ancillary data from radiosondes and ceilometer are introduced. Section ~~5 describes TCWret including a test with synthetic spectra representative for the Arctic to show the performance of TCWret. Section 6~~ 4 gives a brief description of the infrared retrieval TCWret and shows the error estimation for this measurement campaign. Section 5 presents the results of the measurement campaign. After the description of data and code availability, a summary and conclusion ~~is~~ are provided.

2 ~~Area of measurements~~Observations

70 ### 2.1 Area of Measurements

Measurements were performed around Svalbard ~~in 2017~~ from the 24th May 2017 until the 19th August ~~. The measurements with the FTIR were performed during~~ 2017 within the scope of the cruise legs PS106.1 (PASCAL), PS106.2 (SiPCA) and PS107 (FRAM)~~of~~, performed by the RV *Polarstern*. PS106.1 and PS106.2 are collectively referred to as PS106. ~~For further description see~~ The cloud cover was observed by meteorologists of the German Weather Service, who reported a cloud coverage

75 of 7 or 8 oktas in approximately 75% of the time. For further descriptions refer to Macke and Flores (2018) and Schewe (2018). Figure (1) shows the positions of the measurement sites and the ship.
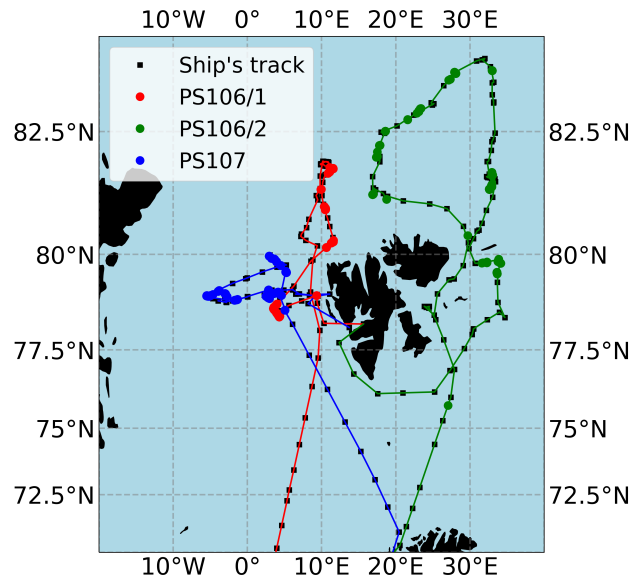
Figure 1. Map of the measurement area. Red markers indicate measurements during PS106.1 (24th May 2017 until 21st June 2017), green markers indicate measurements during PS106.2 (23rd June 2017 until 19th July 2017). Blue markers indicate measurements during PS107 (22nd July 2017 until 19th August 2017). The black line shows the ship's track.
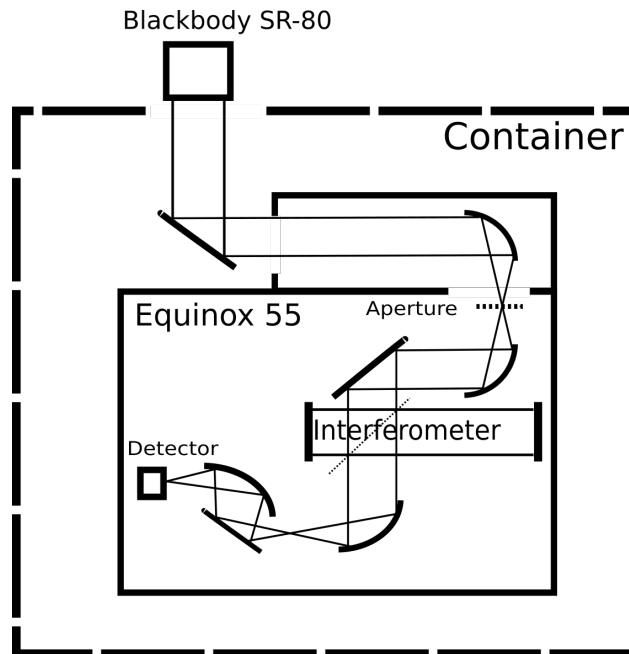
Figure 2. Sketch of the *IFS 55 Equinox*. The blackbody SR-80 can be removed, then atmospheric radiation is measured.

Table 2. Technical specifications of the FTIR spectrometer IFS 55 Equinox.

Beamsplitter	Potassium bromide (KBr)
Detector	Mercury-Cadmium-Tellurium (HgCdT)
Temperature of Detector	Cooled with liquid nitrogen (77 K)
Optical path difference	3 cm
Spectral resolution	$0.3\,\text{cm}^{-1}$
Diameter of entrance arperture	3.5 cm

3 ~~Measurement setup~~

2.1 Measurement setup

Measurements of the atmospheric radiances ~~were~~ are performed with a mobile FTIR spectrometer (IFS 55 Equinox by
~~Bruker~~Bruker-Optics GmbH) in emission mode (~~without using the sun as~~ measures atmospheric radiaton without external light
source), which will be from now on referred to as EM-FTIR. The instrument was located in an air-conditioned and insulated
container on the A-Deck of RV *Polarstern*. The roof of the container ~~has~~ is two openings. Below one opening the EM-FTIR
was located. Both openings ~~could~~ can be closed in case of precipitation. The interferometer inside the FTIR spectrometer has
a movable mirror ~~which gives~~ giving a maximum optical path difference of 3 cm, which results in a maximum spectral reso-
lution of $\Delta\bar{\nu} = 0.3\,\text{cm}^{-1}$. ~~The spectrometer was permanently rinsed~~ To prevent damage on the hygroscopic substance of the
beamsplitter (Potassium bromoide), the spectrometer is permanently purged with dry air. Further specifications are described in
table (2). A blackbody (SR-80 by CI Systems) ~~was~~ is placed manually on the EM-FTIR opening at regular intervals to perform
a radiometric calibration.

2.2 Radiometric calibration and emissivity of the blackbody radiation

To obtain the spectral radiance L_{atm}, a radiometric calibration of the EM-FTIR is necessary. To do so, the blackbody radiator
SR-80 ~~was~~ is used. Its temperature can be set from $-10\,^\circ\text{C}$ to $125\,^\circ\text{C}$~~and has an accuracy of~~. The homogenity of the radiator
surface is better than $\pm 0.05\,\text{K}$. The emissivity of the coating is shown in figure (3). The mean emissivity of the blackbody
radiator is $\varepsilon = 0.976$. An emissivity below 1 means, that the radiaton of the blackbody is a mixture of the Planck radiation at
T_{BB} and the temperature of the container which is assumed to be Planck radiation at T_{lab}. The radiation by the EM-FTIR is
the sum of the radiation of the radiator plus a term which takes into account the temperature of the environment ~~:~~

$$B = \varepsilon B(T_{BB}) + (1 - \varepsilon)B(T_{lab}) \tag{1}$$
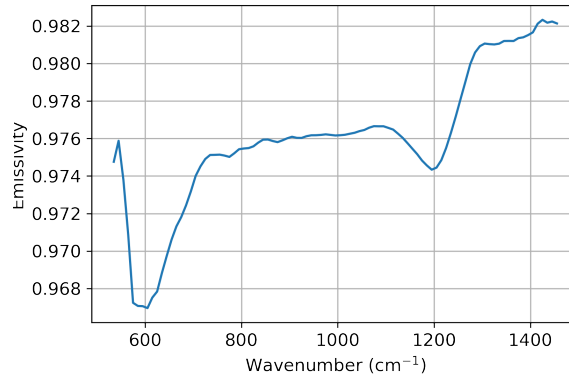
Figure 3. ~~Spectral~~ Smoothed spectral emissivity of the blackbody radiator.

with the temperature of the blackbody T_{BB} and the temperature of the laboratory T_{lab}, weighted by the blackbody emissivity ε (Revercomb et al., 1988).~~The spectrally resolved of the emissivity is shown in figure (3). The mean emissivity of the blackbody radiator is $\varepsilon = 0.976$.~~

100   The ~~blackbody radiator was either heated up to about $100\,^\circ$C or brought to ambient temperature. The~~ radiometric calibration of the spectrometer is performed ~~then~~ using

$$L_{atm} = \varepsilon B_{\bar{\nu}}(T_{amb}) + \varepsilon \frac{B_{\bar{\nu}}(T_{hot}) - B_{\bar{\nu}}(T_{amb})}{\mathcal{F}(I_{hot} - I_{amb})} \cdot \mathcal{F}(I_{atm} - I_{amb}) + (1 - \varepsilon)B_{\bar{\nu}}(T_{lab}) \tag{2}$$

$B(T_{amb,hot,lab})$ are the Planck function ~~of~~ at high temperature (T_{hot}~~), ambient~~, setting to $100\,^\circ$C), surface air temperature (T_{amb}) and at the temperature of the laboratory (T_{lab}). $I_{hot,amb,atm}$ are the ~~inteferograms~~ interferograms of the hot blackbody,

105   blackbody at ambient temperature and the atmospheric measurement. $\mathcal{F}$ is the operator for the Fourier transform. In contrast to the ~~procedere~~ procedure described in Revercomb et al. (1988), here the difference of the interferograms is calculated before applying the Fourier transform.

~~Spectra of the blackbody radiator are measured at high temperature of $T_{hot} \approx 100\,^\circ$C and at ambient temperature T_{amb}.~~ The following cycle ~~was selected~~ is applied for the radiometric calibration: blackbody at T_{hot}, atmospheric radiation, blackbody at

110   T_{amb}, atmospheric radiation, blackbody at T_{hot} and so on. Each measurement cycle of the blackbodies ~~contains 12 individual measurements which are averaged~~ took about 10 minutes to get one blackbody interferogram I_{hot} or I_{amb}. ~~40 measurements of atmospheric radiance were performed in each cycle~~The duration of the atmospheric measurements was approximately 15 minutes. The measurements time and schedule was chosen based on the time it took the blackbody to reach the desired temperature.

115   ## 2.3   OCEANET measurements and Cloudnet synergistic retrieval

Retrievals of microphysical cloud parameters are compared with results of the synergistic retrieval Cloudnet. The OCEANET-Atmosphere observatory from the Leibniz Institute for Tropospheric Research (TROPOS) in Leipzig (Germany) performed

continuous measurements during PS106.1 and PS106.2 (Griesche et al., 2020f). Its container houses a multi-wavelength Raman polarization lidar Polly-XT and a microwave radiometer ~~HATPRO~~ *Humidity and Temperature Profiler (HATPRO)* which was complemented during PS106 by a vertically-pointing motion-stabilized 35-GHz cloud radar Mira-35. The OCEANET measurements provide profiles of aerosol and cloud properties and column-integrated liquid water and water vapor content. To retrieve products like liquid and ice water content the instrument synergistic approach Cloudnet (Illingworth et al., 2007) was applied to these observations. The retrieved Cloudnet dataset during PS106 has been made available via Pangaea (see table 7). As atmospheric input, radiosondes launched from the *RV Polarstern* were used. If no radiosonde is available, radiosondes from Ny-Ålesund (if the ship was neas Svalbard) or model data from the Global Data Assimilation System model (GDAS1) were used. A short summary of the Cloudnet retrieval is given in Appendix A. For a detailed description please refer to Griesche et al. (2020f) and the publications cited there.

3 Atmospheric profiles and cloud height informations

3.1 ~~Cloud ceiling~~

Auxillary data obained in the ship cruise itself were used to construct the atmospheric setup used in the retrieval. This includes temperature and humidity profiles as well as cloud ceiling measurements.

3.1 Cloud ceiling

~~Informations~~ Information about the cloud ceiling ~~were recording~~ was obtained using a Vaisala Ceilometer CL51 operated by the German Weather Service. The maximum cloud detection altitude is $13\,\mathrm{km}$ with a vertical resolution of $10\,\mathrm{m}$~~and a measurement accuracy of $\geq \pm 5\,\mathrm{m}$~~. The uncertainty of the retrieved ceiling is $\pm 1\,\%$, but at least $\pm 5\,\mathrm{m}$. Temporal resolution of the results is $60\,\mathrm{s}$. Although only data of the cloud base height is given, it was decided to use these data instead of the Cloudnet height profile, because the ceilometer data was available during the entire cruise, whereas the Cloudnet measurements were only available for the PS106. Without changing the input data, a consistent dataset for the retrieval should be created. ~~Data~~ However, there is a mean bias between the cloud base height stated by Cloudnet and the ceilometer of $-639\,\mathrm{m}$ (median bias of $-47\,\mathrm{m}$), which means on average the Cloudnet cloud base height is larger than the ceiling given by the ceilometer, and a root-mean-square error of $1870\,\mathrm{m}$. Data of the ceilometer are available at Schmithüsen (2017a), Schmithüsen (2017b) and Schmithüsen (2017c).

3.2 Radiosounding

Radiosondes were launched four times per day (00 UTC, 06 UTC, 12 UTC, 18 UTC) during the PS106 and twice per day (06 UTC and 12 UTC) during the PS107 (Schmithüsen (2017d), Schmithüsen (2017e) and Schmithüsen (2017f)). Data were measured using a RS92 radiosonde by Vaisala. Data of air pressure, temperature, relative humidity, wind speed and wind direction were recorded. Accuracies are $0.5\,\mathrm{K}$ for temperature measurements, $5\,\%$ for relative humidity and $1\,\mathrm{hPa}$ for air pressure. ~~Wind speed and wind direction are not~~ Only atmospheric pressure, temperature and humidity were used here. Atmospheric pro-

files between two radiosonde launches are acquired by linear interpolation. If ~~the~~ a radiosonde stopped measurements before reaching $30\,km$, data were extended using the ERA5 reanalysis (Hersbach et al., 2018).

4 Total Cloud Water retrieval (TCWret)

Total **C**loud **W**ater **ret**rieval (TCWret) is a retrieval algorithm for microphysical cloud parameters from FTIR spectra. It is inspired by MIXCRA (Turner, 2005) and XTRA (Rathke and Fischer, 2000) and uses an optimal estimation approach (Rodgers, 2000) to invert the measured spectral radiances for retrieving microphysical cloud parameters. For a complete description of the retrieval, please refer to appendix B.

4.1 Radiative Transfer Models

Two radiative transfer models are used in TCWret: the Line-By-Line Radiative Transfer Model (LBLRTM) (Clough et al., 2005) and the DIScrete Ordinate Radiative Transfer model (DISORT) (Stamnes et al., 1988). DISORT is called by LBLDIS (Turner, 2005) to calculate spectral radiances.

LBLRTM calculates the optical depth for gaseous absorbers and the water vapour continuum. The profiles of H_2O, CO_2, O_3, CO, CH_4 and N_2O either can be set by the user, or a predefined atmosphere ~~of LBLRTM can be~~ is used. A subarctic summer atmosphere, implemented in LBLRTM, has been used for all gases except H_2O, which has been read from radiosonde measurements.

DISORT calculates the monochromatic radiative transfer through ~~an vertically inhomogenious~~ a vertically inhomogeneous plane-parallel medium including scattering, absorption and emission. ~~DISORT~~ It provides the spectral radiances ~~under given~~ using single-scatter parameters.

~~LBLDIS takes over the calculated optical depths from LBLRTM. Additonally, LBLDIS comes with several databases of single-scatter parameters for liquid water and ice~~ Several databases are included in LBLDIS (Turner, 2014). These databases contain extinction cross sections, absorption cross sections, scattering cross sections, ~~single-scatter~~ single-scattering albedo, asymmetry factor and phase functions for different ~~wavenumber~~ wavenumbers and effective radii. Refractive indices for liquid water droplets and ice crystals are taken from Downing and Williams (1975) and Warren (1984) respectively. Temperature ~~depended~~ dependent refractive indices for liquid water are from Zasetsky et al. (2005). However, it is important to note that they have large uncertainties from $1000\,cm^{-1}$ to $1300\,cm^{-1}$ (Rowe et al., 2013). Scattering properties for more complex ice particle shapes like aggregates, bullet rosettes, droxtals, hollow columns, solid columns, plates and spheroids were calculated by Yang et al. (2001) using a combination of Finite Difference Time Domain (FDTD), geometric optics and Mie theory.

~~The~~ For all liquid droplets and ice crystals, the droplet size distributions follow a gamma size distribution. The gamma size distributions were chosen ~~is~~ in a way, that they fit to the data during the First International Satellite Cloud Climatology Project (ISCCP) Regional Experiment (FIRE) Arctic Cloud Experiment (ACE). For further details, please refer to Turner et al. (2003).

4.2 ~~Working principle of TCWret~~

Microwindows used in TCWret to retrieve the microphysical cloud parameters of this dataset. Interval (cm^{-1})558.5 − 562.0571.0 − 574.07

180   TCWret retrieves optical depths of liquid water and ice water and the effective radii of liquid water droplets and ice crystals from infrared spectral radiances. The retrieval of microphysical cloud parameters is a nonlinear problem, so an iterative algorithm is needed:

$$\boldsymbol{x}_{n+1} = \boldsymbol{x}_n + \boldsymbol{s}_n$$

Here $\boldsymbol{x_n}$ and $\boldsymbol{x_{n+1}}$ are the state vectors containing cloud parameters of the n-th and $(n+1)$-th step and $\boldsymbol{s_n}$ is the modification

185 of the cloud parameters during the n-th iteration. The governing equation to determine $\boldsymbol{s_n}$ is

$$\left(\mathbf{K}_n^T \mathbf{S_y}^{-1} \mathbf{K}_n + \mathbf{S_a}^{-1} + \mu^2 \mathbf{S_a}^{-1}\right) \boldsymbol{s}_n = \mathbf{K}_n^T \mathbf{S_y}^{-1} \left[\boldsymbol{y} - F(\boldsymbol{x}_n)\right] + \mathbf{S_a}^{-1} \cdot (\boldsymbol{x_a} - \boldsymbol{x}_n)$$

. The quantities in the equation are the jacobian matrix $\mathbf{K} = \left(\frac{\partial F(x_i)_j}{\partial x_i}\right)$, the inverse of the variance-covariance matrix $\mathbf{S_y}^{-1}$, the a priori $\boldsymbol{x_a}$ of the cloud parameters and the inverse covariances of the a priori $\mathbf{S_a}^{-1}$, the measured spectral radiances $\boldsymbol{y}$, the calculated spectral radiances $F(\boldsymbol{x_n})$ and the Levenberg-Marquardt term $\mu^2 \cdot \mathbf{S_a}^{-1}$.The aim of the iterations is to minimize the

190 cost function $\xi^2(\boldsymbol{x})$.

$$\xi^2(\boldsymbol{x}_n) = \left[\boldsymbol{y} - F(\boldsymbol{x}_n)\right]^T \mathbf{S_y}^{-1} \left[\boldsymbol{y} - F(\boldsymbol{x}_n)\right] + \left[\boldsymbol{x_a} - \boldsymbol{x}_n\right]^T \mathbf{S_a}^{-1} \left[\boldsymbol{x_a} - \boldsymbol{x}_n\right]$$

Convergence is reached, if the change of the cost function is below a given threshold, here set to 0.1%:

$$\frac{\xi^2(x_{n+1}^2) - \xi^2(x_n)}{\xi^2(x_{n+1})} < 0.001$$

However, convergence in the sense of the cost function does not necessarily mean that the fitted and measured spectrum match.

195 For example, the step size parameter of the Levenberg-Marquardt method could be so large that the cost function changes little. Then the convergence criterion is fulfilled, but the fit does not agree with the measurement. To identify these cases, a reduced-ξ^2-test is performed. This test is used to calculate the distance between calculated and measured radiance, taking into account the variance of the spectrum σ^2. It is defined as

$$\xi^2_{reduced} = DOF \cdot \sum_{n=1}^{N} \frac{y(\bar{\nu}_n) - F(x, \bar{\nu}_n)}{\sigma^2}$$

200 with $DOF =$ number of datapoints - number of parameters. As empirical values, we assume all retrievals with $\xi^2_{reduced} < 1.0$ as converged correctly. Results with $\tau_{liq} + \tau_{ice} > 6$ are excluded.As we do not necessarily have prior informations about the optical depths and effective radii, we decided to set the covariance of the a priori to large values. This shall ensure that the chosen a priori does not constrain the retrieval too strong. Initial values and a priori are set to equal values: $\boldsymbol{x} = (0.25, 0.25, \log(5.0), \log(20.$ The logarithm was chosen so that all entries of $\boldsymbol{x}$ have similar size. The variance-covariance matrix of the a priori is set to

205 $$\mathbf{S_a}^{-1} = \begin{pmatrix} 0.04 & 0 & 0 & 0 \\ 0 & 0.04 & 0 & 0 \\ 0 & 0 & 0.047 & 0 \\ 0 & 0 & 0 & 0.047 \end{pmatrix}$$

~~. Variances in $\mathbf{S_y}^{-1}$ are calculated from the spectral region between $1925\,\mathrm{cm}^{-1}$ and $2000\,\mathrm{cm}^{-1}$, where no signal from the atmosphere is expected. The variance-covariance matrix is assumed to be diagonal: $\mathbf{S_y} = \sigma^2 \mathbf{I}$. It is assumed to be the variance of the scene. To retrieve cloud parameters, only radiance from spectral intervals given in table (B1) is used.~~

4.2 Products of TCWret

210   Direct retrieval products are τ_{liq}, τ_{ice}, r_{liq} and r_{ice}. From these parameters the water paths are calculated:

$$LWP = \frac{2}{3} \cdot r_{liq} \cdot \tau_{liq} \cdot \varrho_{liq} \tag{3}$$

$$IWP = \frac{N \cdot V_0(r_{ice}) \cdot \tau_{ice}}{\sigma_{ice}} \frac{N \cdot V_0(r_{ice}) \cdot \tau_{ice}}{\alpha_{ice}} \cdot \varrho_{ice} \tag{4}$$

with the volumetric mass densities of liquid water $\varrho_{liq} = 1000\,\mathrm{kg} \cdot \mathrm{m}^{-3}$, ice water $\varrho_{ice} = 917\,\mathrm{kg} \cdot \mathrm{m}^{-3}$, the particle number density N and the ~~extincion coefficient $\sigma_{ice} = ext(r_{ice}) \cdot N$~~ extinction coefficient $\alpha_{ice} = \beta_{ice} \cdot N$. The total volume of an ice
215   crystal $V_0(r_{ice})$ and the extinction cross section of an ice droplet ~~$ext(r_{ice})$~~ β_{ice}, both integrated over the gamma size distribution are read from the databases of single-scattering parameters. The formula for the liquid water path works for spherical droplet only, while the formula for the ice water path is valid for ice crystals of any shape (Turner, 2005). The covariance matrix $\mathbf{S}_r$ of the optimal estimation procedure is used to determine the errors.

4.3 Covariance matrix and averaging kernels

220   Retrieval errors are calculated from the variance-covariance matrix $\mathbf{S}_r$ of the retrieval. It is calculated by

$$\mathbf{S}_r = \mathbf{T}_r \mathbf{S}_y \mathbf{T}_r^T \tag{5}$$

~~.~~ The index r denotes quantities of the final iteration. $\mathbf{T}$ is a transfer matrix and $\mathbf{S}_y$ is the variance-covariance matrix of the measurement. The retrieval uses a Levenberg-Marquardt algorithm, therefore the variance-covariance matrix and the transfer matrix $\mathbf{T}$ are calculated iteratively, as described by Ceccherini and Ridolfi (2010). ~~In brief: In each step the transfer matrix $\mathbf{T}$~~
225   ~~is calculated taking into account the current step size parameter μ by~~

$$\begin{cases} \mathbf{T_0} = \mathbf{0} \\ \mathbf{T}_{i+1} = \mathbf{G}_i + \left(\mathbf{I} - \mathbf{G}_i \mathbf{K}_i - \mathbf{M}_i \mathbf{S}_a^{-1} \right) \mathbf{T}_i \end{cases}$$

~~with $\mathbf{0}$ as zero matrix and $\mathbf{I}$ as identity matrix. $\mathbf{M}_i$ is the term in the brackets on the left side of (B3) and $\mathbf{G}_i = \mathbf{M}_i \mathbf{K}_i^T \mathbf{S}_y^{-1}$.~~
~~Diagonal elements of $\mathbf{S}_r$ are the variances of the final cloud parameters.~~ Another important quantity to characterize the retrieval quality is the Averaging Kernel Matrix $\mathbf{A}$. The averaging kernel matrix contains the derivatives of the retrieved quantities with
230   respect to the true state vector

$$\mathbf{A} = \frac{\partial \boldsymbol{x_r}}{\partial \boldsymbol{x_t}} \tag{6}$$

, where x_r means the retrieved parameters and x_t are the unknown true parameters. In TCWret, the averaging kernel matrix is a 4×4-matrix. The top two rows belong to τ_{liq} and τ_{ice}, the bottom two rows belong to r_{liq} and r_{ice}. On the diagonal elements one finds the derivatives of each element in the retrieved state vector with respect to its corresponding element in the true state vector. Off-diagonal elements give the degree of correlation between the entries of the state vector

$$
\mathbf{A} = \begin{pmatrix}
A_{\tau_{liq}} & A_{\tau_{liq},\tau_{ice}} & A_{\tau_{liq},r_{liq}} & A_{\tau_{liq},r_{ice}} \\
A_{\tau_{ice},\tau_{liq}} & A_{\tau_{ice}} & A_{\tau_{ice},r_{liq}} & A_{\tau_{ice},r_{ice}} \\
A_{r_{liq},\tau_{liq}} & A_{r_{liq},\tau_{ice}} & A_{r_{liq}} & A_{r_{liq},r_{ice}} \\
A_{r_{ice},\tau_{liq}} & A_{r_{ice},\tau_{ice}} & A_{r_{liq},r_{ice}} & A_{r_{ice}}
\end{pmatrix}
\tag{7}
$$

Here $A_{v,w}$ stands for the mutual dependence of the parameters v and w, where v is the parameter in x_r and w is the parameter in x_t. The trace of the averaging kernel matrix gives the degrees of freedom of the signal, which can be interpreted as the number of individually retrievable parameters from the measurement (Rodgers, 2000). The averaging kernel matrix sets the retrieval and the a priori into context:

$$
x_r = x_a + \mathbf{A}(x_t - x_a)
\tag{8}
$$

From this relationship it can be seen that in the optimal case the Averaging Kernel Matrix is the unit matrix. Smaller entries mean a stronger influence by the a priori. Averaging kernels in TCWret are calculated via

$$
\mathbf{A} = \mathbf{T}_r \mathbf{K}_r
\tag{9}
$$

(Ceccherini and Ridolfi, 2010). Errors The matrix $\mathbf{K}_r$ is the jacobian matrix of the retrieved parameters (Ceccherini and Ridolfi, 2010). Uncertainties of LWP and IWP are calculated from error propagation:

$$
\sigma_Y = \pm \sqrt{\sum_i \left(\frac{\partial Y}{\partial m_i} \sigma_{m_i} \right)^2}
\tag{10}
$$

where Y is either LWP or IWP, $\frac{\partial Y}{\partial m}$ is the partial derivative of Y with respect to an atmospheric parameter $m = \{\tau_{liq}, \tau_{ice}, r_{liq}, r_{ice}\}$ and σ_{m_i} is the variance of the i-th parameter m_i, as stated in $\mathbf{S_r}$.

4.4 Retrieval performancePerformance of TCWret applying to simulated data

A set of synthetic testcases containing spectral radiances of artifical clouds with known cloud parameters, created by Cox et al. (2016), will be used to test the ability of TCWret to retrieve $\tau_{liq}, \tau_{ice}, r_{liq}$ and r_{ice}. Additionally, the derived quantities LWP and IWP are discussed. This dataset contains several representative cases of Arctic clouds. Clouds are set to be either vertically homogenous, topped by a layer of liquid water or with thin boundaries. Ice crystal shapes are mostly set to be spheres, but some cases where calculated with hollow columns, solid columns, bullet rosettes or plates. All spectra are convoluted with a sinc-function to the resolution of the IFS 55 Equinox ($0.3\,\mathrm{cm}^{-1}$) and perturbed by a Gaussian distributed noise of

Table 3. Results of the testcase retrievals. $|r|$ is the correlation coefficient of each quantity. Mean ~~bias~~ is the mean difference between retrieval and the true size of the parameter. ~~STD (TC)~~ RMSE is the ~~standard deviation~~ root-mean-square of the difference between retrieval and true parameter. For $\tau_{liq,ice}$ and $r_{liq,ice}$, ERR (OE) is the standard deviation ~~provided by~~ calculated from the posterior covariance matrix of the optimal estimation ~~without covariances~~, stated in equation ($\tau_{liq,ice}, r_{liq,ice}$ 5) ~~or the standard deviation from propagation of uncertainty using~~ . For the ~~variances (LWP, IWP, τ_{cw}, f_{ice}~~ other quantities, $\bar{r}$ ERR(OE) is calculated by error propagation. *Maximum of quantity in testcases specifies* the maximum value that can be used for this quantity in the test cases. A total number of 253 testcases are included in these calculations.

Quantity	$\|r\|$	Mean ~~bias~~ Bias	~~STD (TC)~~ RMSE	ERR (OE)	Maxi
τ_{liq} (1)	0.86	~~−0.08~~ −0.1	~~0.52~~ 0.5	~~0.34~~ 0.3	
τ_{ice} (1)	0.78	~~0.19~~ 0.2	~~0.56~~ 0.6	~~0.32~~ 0.3	
$\tau_{cw} = \tau_{liq} + \tau_{ice}$ (1)	0.99	~~0.11~~ 0.1	~~0.17~~ 0.2	~~0.67~~ 0.7	
f_{ice} (1)	0.70	0.08	~~0.25~~ 0.3	~~0.59~~ 0.6	
r_{liq} (µm)	0.59	~~−2.37~~ −2.4	~~3.35~~ 4.1	~~2.93~~ 2.9	
r_{ice} (µm)	0.65	~~2.94~~ 3.0	~~9.68~~ 10.0	~~2.39~~ 2.4	
~~$\bar{r} = (1 - f_{ice}) \cdot r_{liq} + f_{ice} \cdot r_{ice}$ (µm) 0.80 1.75 5.75 14.30 56.82~~ LWP (g·m^{-2})	0.68	~~−1.85~~ −1.9	~~6.01~~ 6.3	~~2.31~~ 2.3	
IWP (g·m^{-2})	0.82	~~1.91~~ 1.9	~~9.85~~ 10.0	~~5.06~~ 5.1	

~~1 mW·(sr·cm^{-1}·m^{-2})$^{-1}$: We modified the spectral radiance at each wavenumber by drawing a random number from a normal distribution with the true spectral radiance as mean of the distribution and 1 mW·(sr·cm^{-1}·m^{-2})$^{-1}$ as its standard deviation. This value has been chosen, because it is near the observed standard deviation of the real spectra from the measurement~~

260 ~~campaign of 0.82 mW·(sr·cm^{-1}·m^{-2})$^{-1}$. Ice crystals are chosen to be spheres, thus only the testcases which are calculated with spherical ice crystals are used here. The influence of the chosen ice particle form will be adressed later. Table (3) gives the correlation coefficients, mean deviations and standard deviations between the retrieved cloud parameters~~ In addition to the uncertainties indicated by the optimal estimation procedure, TCWret was applied to simulated data (Cox et al., 2016). The description of the testcases and the ~~true cloud parametern. Additionally, the stndard deviation calculated via the variance-covariance~~

265 ~~matrix is given. In all cases, a significant correlation can be observed. This means, TCWret can retrieve all of the parameters from the testcases under the given uncertainties. Of all direct retrieval products, the optical depths τ_{liq} and τ_{ice} have the highest agreement to the true cloud parameters. For the liquid phase, the difference to the true optical depths is (-0.08 ± 0.52). For the optical depth of the ice phase, the difference is larger with (0.19 ± 0.56). Since τ_{liq} and τ_{ice} include both optical depths and phase, the optical depth of the condensed water $\tau_{cw} = \tau_{liq} + \tau_{ice}$ as well as the fraction of ice in the optical depth~~

270 ~~$f_{ice} = \tau_{ice} \cdot \tau_{cw}$ are calculated. Here it becomes clear that the optical depth can be determined accurately ($|r| = 0.99$, mean and~~

standard deviation (0.11 ± 0.17)). It then also follows that the deviations of τ_{liq} and τ_{ice} come from the phase determination. The deviation for the phase is (0.08 ± 0.25) with a correlation coefficient of $|r| = 0.70$. When considering the effective radii, only results of r_{liq} were used in where f_{ice} is less than 0.9. For r_{ice} only results with $f_{ice} > 0.1$ are considered. The mean difference of the retrieval from the true parameters is the standard deviations are (-2.37 ± 3.35) for r_{liq} and (2.94 ± 9.68) for r_{ice}. Additionally, the quantity $\bar{r} = (1 - f_{ice}) \cdot r_{liq} + f_{ice} \cdot r_{ice}$ is calculated. It can be interpreted as the mean effective radius for liquid droplets and ice crystals of the entire cloud. For $\bar{r}$, the difference to the testcases is $(1.75 \pm 5.75)\,\mathrm{\mu m}$ with a correlation coefficient of $|r| = 0.80$. Therefore, $\bar{r}$ can be estimated independently from its constituents r_{liq}, r_{ice} and f_{ice}. For example, a too large r_{ice} can lead to an underestimation of r_{liq} and vice versa. The mean averaging kernel matrix over all retrievals is

$$\mathbf{A} = \begin{pmatrix} 0.87 & 0.09 & -0.15 & -0.09 \\ 0.11 & 0.90 & 0.19 & 0.03 \\ -0.04 & 0.07 & 0.50 & 0.05 \\ -0.16 & 0.05 & 0.03 & 0.42 \end{pmatrix}$$

The top two rows belong to τ_{liq} and τ_{ice}, the bottom two rows belong to r_{liq} and r_{ice}. From equation (8) can be seen that the diagonal elements show for each parameter how strong the retreived parameter is influenced by the a priori. Whereas the diagonal elements of the optical depths are near 1, indicating independence from the a priori, results for r_{liq} and r_{ice} show a larger influence from the a priori. From the trace of the averaging kernels follow 2.69 degrees of freedom of the signal. Therefore, additional information that limits the number of independent quantities to be determined can improve the retrieval. The water paths are calculated from the optical depths and effective radii, therefore both quantities are influenced by the phase determination, as seen before in $\tau_{liq,ice}$ and $r_{liq,ice}$. The difference from the testcases is (-1.85 ± 6.01) for the LWP and (1.91 ± 9.85) for the IWP. However, the standard deviation for the LWP is less than the standard deviation observed for LWP from microwave radiometer of at least $15\,\mathrm{g \cdot m^{-2}}$ (Löhnert and Crewell, 2003). Standard devations given by the variance-covariance matrix of the retrieval are shown in table (3) and named as ERR(OE). ERR(OE) is below STD(TC) for $\tau_{liq,ice}, r_{liq,ice}$, LWP and IWP. This might be due to uncertainties from the forward model, which are neglected here, propagated into the retrievals or due to the assumption of a diagonal variance matrix $\mathbf{S_y}$. To address the effect of these differences in the uncertainties, ERR(OE) is scaled so it matches STD(TC) evaluation can be found in the appendix C. Results are shown in table (3). When applied to the simulated data, it could be shown that TCWret can determine all variables entered in the table. Results calculated by TCWret are comparable to the true cloud parameters from the simulated data.

4.5 Erorrs of atmospheric profile and calibration

Besides the uncertainties from the optimal estimation algorithm, uncertainties from atmospheric profile data and the calibration cycle increate the total uncertainty of the data.

Table 4. ~~Standard deviations of~~ Mean partial derivatives, used for estimating ~~the~~ ~~differences between retrievals without parameter errors and retrievals with~~ parameter errors Δpar.

Quantity m	$\sigma_T \frac{\partial m}{\partial T}$	$\sigma_q \frac{\partial m}{\partial q}$	$\sigma_L \frac{\partial m}{\partial L}$
τ_{liq} ~~(1)~~ ~~0.31~~	0.03	~~0.07~~ 0.02	-0.01
τ_{ice} ~~(1)~~	~~0.32~~ 0.12	~~0.02~~ -0.01	~~0.08~~ -0.02
r_{liq} ~~(µm)~~	~~2.14~~ -0.58	~~0.27~~ 0.14	~~3.33~~ -1.97
r_{ice} ~~(µm)~~	~~5.23~~ 1.38	~~1.00~~ 0.62	~~15.76~~ -7.01
LWP ~~(g · m^{-2})~~	~~2.84~~ -0.27	~~0.25~~ 0.15	~~1.35~~ -0.47
IWP ~~(g · m^{-2})~~	~~5.64~~ 2.43	~~0.64~~ 0.14	~~3.11~~ -1.41
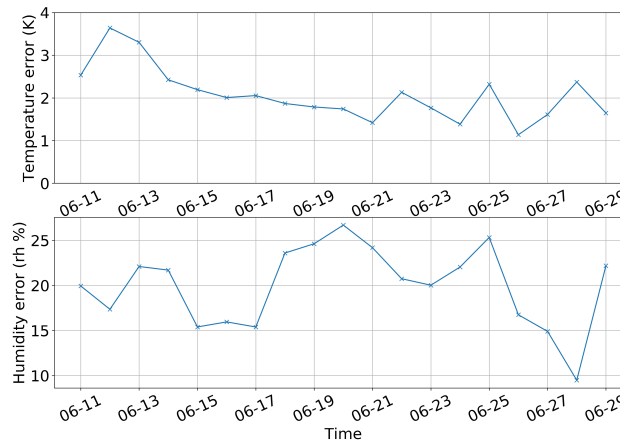
Figure 4. ~~Combined~~ Total error as sum of device error and interpolation error.

4.6 ~~Erorrs of atmospheric profile and calibration~~

4.5.1 Partial derivatives for non-retrieved quantities

~~For estimating the propagation of errors of the humidty profile, cloud temperatureand emissivity and temperature of the blackbody radiator into the cloud parameters, cloud parameters from the testcases have been retrieved. In contrast to the section of the retrieval performance, following modifications were perfomed~~ To estimate the uncertainty which comes from the cloud temperature, humidity profile and spectral calibration, the testcases from Cox et al. (2016) have been adjusted to incorporate uncertainties in cloud temperature, humidity and radiance. Three datasets are creating, each of them with one of the following adjustments:

14

- Increase cloud temperature by $1\,\mathrm{K}$

- Increase atmospheric humidity by $10\,\%$

- Increase radiance by $2\,\mathrm{mW} \cdot (\mathrm{cm}^{-1} \cdot \mathrm{m}^2 \cdot \mathrm{sr})^{-1}$

310 ~~These errors will be called *parameter errors*. Each of these modifications is applied individually, creating three new datasets~~ With these datasets the partial derivatives are calculated, which are necessary to determine the errors due to cloud temperature, humidity and spectral calibration and propagate them into the retrieved cloud parameters by application of

$$\Delta m = \pm \sqrt{\left(\frac{\partial m}{\partial T}\Delta T\right)^2 + \left(\frac{\partial m}{\partial q}\Delta q\right)^2 + \left(\frac{\partial m}{\partial L}\Delta L\right)^2} \tag{11}$$

with the cloud temperature T, the relative humidity q, the radiance L and their errors ΔT, Δq and ΔL. To separate the influence

315 of the parameter errors from the retrieval performance, the results of ~~the parameter error-data~~ these three datasets are compared to the ~~dataset calculated by TCWret to determine the retrieval performance~~ retrieval results mentioned in section 4.3 instead of the true cloud parameters. ~~For each testcase,~~ Mean partial derivatives are then calculated as follows:

1. Retrieve the cloud parameters for each dataset

2. Calculate the difference between the ~~retrieval results with parameter error and without parameter error is determined.~~

320 ~~As an estimate of the error of each atmospheric parameter, the standard deviation of all differences is calculated. The standard deviations per unit size~~ cloud parameters of the adjusted dataset and the undisturbed dataset (which has been already used in section 4.3)

3. Calculate the difference quotients, which will act as partial derivates in equation (11)

The partial derivatives are shown in table (~~??). Then, the parameter error is~~

325 ~~$\Delta par = \pm \sqrt{(\sigma_T \Delta T)^2 + (\sigma_q \Delta q)^2 + (\sigma_L \Delta L)^2}$~~

~~with the cloud temperature T, the relative humidity q, the radiance L and their errors ΔT, Δq and ΔL.~~ 4).

4.5.2 Temperature and humidity

Device errors of the radiosonde are ~~$\Delta T = 0.5\,\mathrm{K}$~~ $\Delta T = 0.5\,\mathrm{K}$ and $\Delta q = 5\,\%$. Additionally, the error introduced with the linear interpolation of the temperature and relative humidity ~~must be estimated . To estimate this interpolation error , the~~

330 ~~interpolated profile is compared with the vertical profile of the corresponding variables of the~~ is estimated by comparing the interpolated profiles to atmospheric profiles from ERA5. The interpolation error follows from the comparison between the linear interpolation between two radiosonde measurements and the ERA5 ~~reanalysis. The standard deviation of the difference of the profiles is interpreted as the interpolation error. Figures~~ atmosphere at the position of the measurements. We query the ERA5 atmosphere for each hour. Then we calculate the atmospheric profiles from the radiosondes once per hour by linear

15

interpolation. From this we calculate the difference, average over one day and calculate the standard deviation. Figure (4) gives the ~~combined~~ total error as device error and interpolation error, as an example for the period from 11th June 2017 to 30th June 2017.

4.5.3 Calibration error

The accuracy of the blackbody temperature and emissivity are $\Delta T_{BB} = \pm 0.05\,\mathrm{K}$ and $\Delta \epsilon = \pm 0.02$. The propagation of these errors into the radiance is ~~performed by~~

$$\Delta L = \sqrt{\left(\frac{\partial L_{atm}}{\partial \epsilon} \cdot 0.02\right)^2 + \left(\frac{\partial L_{atm}}{\partial T_{BB}} \cdot 0.05\,\mathrm{K}\right)^2} \tag{12}$$

To estimate $\frac{\partial L_{atm}}{\partial \epsilon}$, a spectrum is calibrated with an emissivity of ~~ε' and $\varepsilon' + h$. The differential quotient~~ ϵ' and $\epsilon' + h$. The partial derivative is calculated by $\frac{\partial L_{atm}}{\partial \epsilon} = \frac{L(\varepsilon'+h)-L(\varepsilon')}{h}$ with ~~the~~ $L(\varepsilon')$ ~~as~~, the radiance under the emissivity ε' ~~. From $\epsilon = 0.975$~~ and h as step size for the numerical calculation of the partial derivative. From $\epsilon' = 0.975$ and $h = 0.02$ follows $\frac{\partial L_{atm}}{\partial \epsilon} \cdot 0.02 = -0.98\,\mathrm{mW} \cdot (\mathrm{sr} \cdot \mathrm{cm}^{-1} \cdot \mathrm{m}^2)^{-1}$. The second ~~differential quotient~~ partial derivative $\frac{\partial L_{atm}}{\partial T_{BB}}$ is estimated using equation (2). The emissivity is set to 1. The measured radiance of the hot blackbody is larger than the radiance of the atmosphere (~~$\mathcal{F}(I_{hot}) > \mathcal{F}I_{atm}$~~ $\mathcal{F}(I_{hot}) > \mathcal{F}(I_{atm})$) and therefore the quotient $\frac{\mathcal{F}(I_{hot}-I_{amb})}{\mathcal{F}(I_{atm}-I_{amb})} < 1$. ~~Setting $\frac{\mathcal{F}(I_{hot}-I_{amb})}{\mathcal{F}(I_{atm}-I_{amb})} = 1$ as an upper limit, equation~~

$$\frac{\mathcal{F}(I_{atm} - I_{amb})}{\mathcal{F}(I_{hot} - I_{amb})} < 1 \tag{13}$$

From the measurements it follows that L_{hot} is about five times larger than L_{amb}, therefore there inequtaion (13) is set $\frac{\mathcal{F}(I_{hat}-I_{amb})}{\mathcal{F}(I_{hot}-I_{amb})} = 0.2$. Equation (2) thus can be written as $L = B_{\bar\nu}(T_{hot})$. ~~Thus, the estimation of the radiance error caused by temperature uncertainties depends on the temperature of the hot blackbody. With $T_{BB} = T_{hot} = 100\,\mathrm{K}$~~

$$L_{atm} = B_{\bar\nu}(T_{amb}) + 0.2 \cdot B_{\bar\nu}(T_{hot}) - B_{\bar\nu}(T_{amb}) \tag{14}$$

With $T_{BB} = T_{hot} = 100\,°\mathrm{C}$ and $T_{amb} = 0\,°\mathrm{C}$ is $\frac{\partial L_{atm}}{\partial T_{BB}} \cdot 0.05 = 0.10\,\mathrm{mW} \cdot (\mathrm{sr} \cdot \mathrm{cm}^{-1} \cdot \mathrm{m}^2)^{-1}$ as an average for the spectral interval between $500\,\mathrm{cm}^{-1}$ and $2000\,\mathrm{cm}^{-1}$. This gives ~~$\Delta L = 0.99\,\mathrm{mW} \cdot (\mathrm{sr} \cdot \mathrm{cm}^{-1} \cdot \mathrm{m}^2)^{-1}$. Setting $\Delta T = 2\,\mathrm{K}$, $\Delta q = 17.5\%$~~ $\Delta L = 0.98\,\mathrm{mW} \cdot (\mathrm{sr} \cdot \mathrm{cm}^{-1} \cdot \mathrm{m}^2)^{-1}$.

4.5.4 Resulting parameter error

Finally, from the calculations in this section, the resulting unvertaities are

- $\Delta T = 2.0\,\mathrm{K}$, as sum of the device error ($0.5\,\mathrm{K}$) and ~~$\Delta L = 0.99\,\mathrm{mW} \cdot (\mathrm{sr} \cdot \mathrm{cm}^{-1} \cdot \mathrm{m}^2)^{-1}$ gives $\Delta \tau_{liq} = 0.82$, $\Delta \tau_{ice} = 0.77$, $\Delta r_{liq} = 7.21\,\mu\mathrm{m}$, $\Delta r_{ice} = 25.63\,\mu\mathrm{m}$~~ the interpolation error ($1.5\,\mathrm{K}$)

- $\Delta q = 17.5\%$, as sum of the device error (5.0%) and the interpolation error (12.5%)

– $\Delta L = 0.98\,\mathrm{mW} \cdot (\mathrm{sr} \cdot \mathrm{cm}^{-1} \cdot \mathrm{m}^2)^{-1}$

Applying these uncertainties to equation (11), $\Delta LWP = 7.27\,\mathrm{g} \cdot \mathrm{m}^{-2}$ the uncertainties for each parameter are $\Delta\tau_{liq} = 0.4$, $\Delta\tau_{ice} = 0.3$, $\Delta r_{liq} = 3.3\,\mu\mathrm{m}$, $\Delta r_{ice} = 13.1\,\mu\mathrm{m}$, $\Delta LWP = 2.8\,\mathrm{g} \cdot \mathrm{m}^{-2}$ and $\Delta IWP = 16.21\,\mathrm{g} \cdot \mathrm{m}^{-2}$.

4.6 Results for different ice particle shapes

Standard deviations for the difference of r_{ice} with different ice crystal shapes. Shapes are spheres (SPH), aggregates (A), bullet rosette (BR), droxtals (D), hollow columns (HC), plates (P), solid columns (SC) and spheroids (SPO). Bold numbers show standard deviations which exceed the standard deviation of r_{ice} from the testcases (9.68 µm). SPH A BR D HC P SC SPOSPH 6.76 **14.15** 4.17 4.62 **10.72** 3.88 3.18 A 6.76 **12.14** 6.76 5.60 9.50 6.58 6.86BR **14.15 12.14 13.78 12.89 14.52 13.45 13.84**D 4.17 6.76 **13.78** 4.78 **10.88** 2.99 3.67HC 4.62 5.60 **12.89** 4.78 **10.19** 4.47 4.52P **10.72** 9.50 **14.52 10.88 10.19 10.84 11.07**SC 3.88 6.58 **13.45** 2.99 4.47 **10.84** 3.56SPO 3.18 6.86 **13.84** 3.67 4.52 **11.07** 3.56

Standard deviations for the difference of IWP with different ice crystal shapes. Shapes are spheres (SPH), aggregates (A), bullet rosette (BR), droxtals (D), hollow columns (HC), plates (P), solid columns (SC) and spheroids (SPO). Bold numbers show standard deviations which exceed the standard deviation of IWP from the testcases (9.85 g·m^{-2}). SPH A BR D HC P SC SPOSPH 7.58 9.31 4.37 6.00 7.80 3.90 3.39A 7.58 8.32 7.08 6.80 7.29 7.04 7.79BR 9.31 8.32 9.13 8.85 9.13 9.08 9.72D 4.37 7.08 9.13 6.49 7.37 4.20 4.93HC 6.00 6.80 8.85 6.49 8.04 6.27 5.71P 7.80 7.29 9.13 7.37 8.04 6.99 8.45SC 3.90 7.04 9.08 4.20 6.27 6.99 4.43SPO 3.39 7.79 9.72 4.93 5.71 8.45 4.43

Standard deviations for the difference of τ_{ice} with different ice crystal shapes. Shapes are spheres (SPH), aggregates (A), bullet rosette (BR), droxtals (D), hollow columns (HC), plates (P), solid columns (SC) and spheroids (SPO). Bold numbers show standard deviations which exceed the standard deviation of τ_{ice} from the testcases (0.56). SPH A BR D HC P SC SPOSPH 0.49 **0.57** 0.39 0.38 0.49 0.36 0.30A 0.49 0.39 0.43 0.41 0.36 0.41 0.47BR **0.57** 0.39 0.51 0.47 0.37 0.52 0.55D 0.39 0.43 0.51 0.41 0.46 0.37 0.40HC 0.38 0.41 0.47 0.41 0.42 0.37 0.36P 0.49 0.36 0.37 0.46 0.42 0.41 0.48SC 0.36 0.41 0.52 0.37 0.37 0.41 0.36SPO 0.30 0.47 0.55 0.40 0.36 0.48 0.36

Without the ability to retrieve the ice shape from the spectral radiances, the data from the measurement campaign is used to investigate the choice of the ice crystal shape on the retrieval results. Table (**??**) shows the standard deviations of r_{ice} for various ice crystal shapes. In particular, the retrievals with bullet rosettes and plates strongly deviate from the other results. The standard deviation for bullet rosettes is always above that of the test cases. For plates, it is only lower with aggregates, at 9.50 g·m^{-2}. From this it can be concluded that an incorrect choice of ice shape causes a particularly large error if the ice crystals are of the shape bullet rosette or plate or if the retrieval incorrectly uses bullet rosette or plate although the ice crystals have a different shape.Unlike r_{ice}, τ_{ice} is less strongly influenced by the ice crystal shape. Results for τ_{ice} are shown in table (**??**). Largest standard deviation occurs in the cases of bullet rosettes and aggregates.In table (**??**)are the standard deviations for the differentials of IWP with different ice crystal shapes. Again, the standard deviations for bullet rosettes and plates are larger than for the other ice particle shapes. The standard deviation of 9.85 g·m^{-2} calculated from the testcases is not exceeded in any case. Thus, the IWP is less susceptible to an incorrectly chosen ice crystal shape than r_{ice}. This can also be deduced from

17
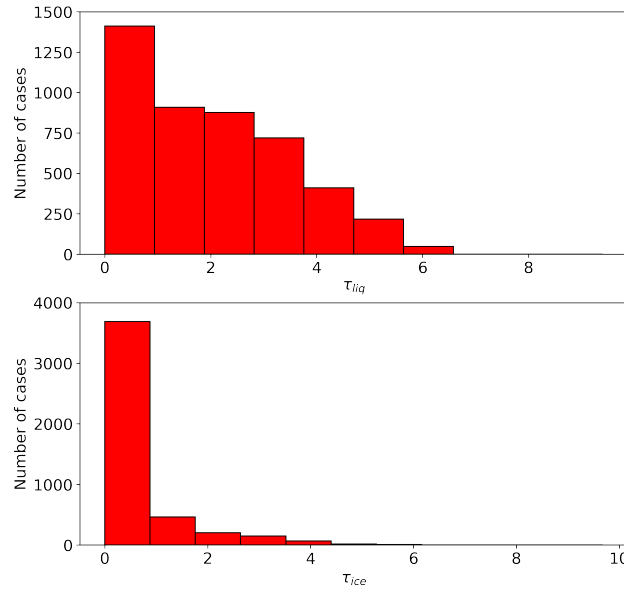
Figure 5. Distribution of ~~retreived~~ retrieved optical depths for liquid water (upper ~~plot~~panel) and ice water (lower ~~plot~~panel). The binwidth is set to the sum of the root-mean-square from table (3) and the errors discussed in section 4.5.

~~equation (4), since in addition to r_{ice}, τ_{ice} is also included in the calculation of the IWP, which reacts less strongly to the shape of the ice crystals than r_{ice}~~$\Delta IWP = 5.6\,\mathrm{g} \cdot \mathrm{m}^{-2}$. These values will be added to the retrieval errors in the next section.

5 Results

5.1 ~~Statistics of optical depths, effective radii~~ Cloud parameters from infrared radiance measurements during the PS106 ~~and water paths~~and PS107

~~The dataset is published at Pangaea (Richter et al., 2021).~~

During the measurement campaign, most of the observed optical depth is due to liquid water insted of ice crystals. A histogram of all retrieved optical depths ~~is~~ are shown in figure (5). In $66.4\,\%$ of the measurements, ice was observed in the clouds, whereas in $92.4\,\%$ of the measurements liquid water was present. Mean optical depths are ~~$\tau_{liq} = 2.64$ and $\tau_{ice} = 0.81$~~$\tau_{liq} = 2.6$ and $\tau_{ice} = 0.8$. Similar to the optical depth, most of the observed cloud water is liquid water (figure 6). Here the means are ~~$LWP = 17.68\,\mathrm{g} \cdot \mathrm{m}^{-2}$ and $IWP = 9.92\,\mathrm{g} \cdot \mathrm{m}^{-2}$~~$LWP = 17.7\,\mathrm{g} \cdot \mathrm{m}^{-2}$ and $IWP = 9.9\,\mathrm{g} \cdot \mathrm{m}^{-2}$. Interquartile ranges for LWP and IWP are ~~$IQR_{LWP} = 18.90\,\mathrm{g} \cdot \mathrm{m}^{-2}$ and $IQR_{IWP} = 11.53\,\mathrm{g} \cdot \mathrm{m}^{-2}$~~$IQR_{LWP} = 18.9\,\mathrm{g} \cdot \mathrm{m}^{-2}$ and $IQR_{IWP} = 11.5\,\mathrm{g} \cdot \mathrm{m}^{-2}$. Whereas the range of LWP matches the LWP from the testcases, the IWP is near the lower threshold of the retrievable water path.

The distributions of the effective radii ~~is~~ are shown in figure (7). For r_{liq} only cases with $f_{ice} < 0.9$ are used ~~. Similar~~ and for
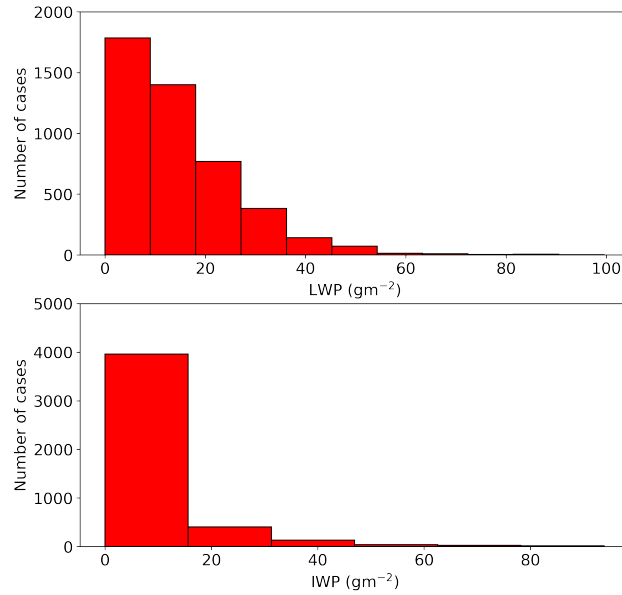
Figure 6. Distribution of retrieved LWP (upper ~~plot~~panel) and IWP (lower ~~plot~~panel). The binwidth is set to the sum of the root-mean-square from table (3) and the errors discussed in section 4.5.

Table 5. Key features of the dataset

Key figure	Size
Retrievals performed	5564
Accepted retrievals	4590
Mixed-phase clouds ($0.1 < f_{ice} < 0.9$)	2158
Single-phase liquid ($f_{ice} < 0.1$)	2899
Single-phase ice ($f_{ice} > 0.9$)	507
Minimum observed precipitable water vapour (PWV)	0.67 cm
Maximum observed precipitable water vapour (PWV)	1.62 cm

r_{ice} ~~, where~~ only cases with $f_{ice} > 0.1$ are used. On average, ice crystals ($r_{ice} = 22.33\,\mu m$ $r_{ice} = 22.3\,\mu m$) are larger than liquid droplets ($r_{liq} = 10.88\,\mu m$ $r_{liq} = 10.9\,\mu m$). Ice crystals show a wider range of retrieved effective radii than liquid droplets, expressed by an interquartile range of ~~$IQR_{ice} = 17.89\,\mu m$ compared to $IQR_{liq} = 5.92\,\mu m$.~~ $IQR_{ice} = 17.9\,\mu m$ compared to
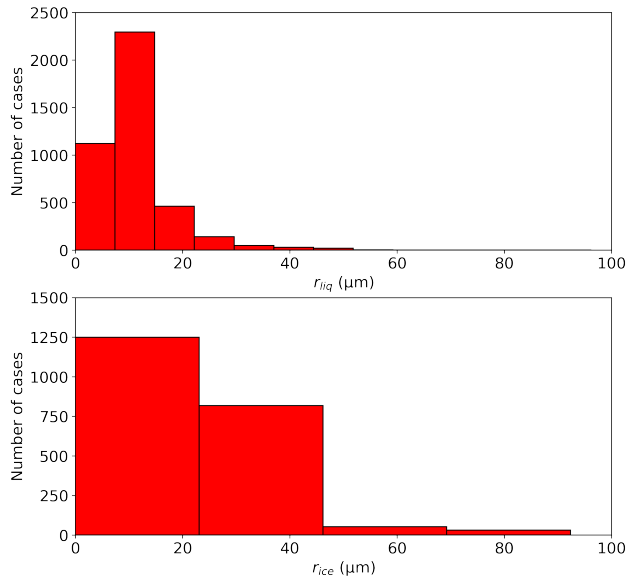
Figure 7. ~~Distributin~~ <u>Distribution</u> of retrieved effective radii for liquid water droplets (upper ~~plot~~<u>panel</u>) and ice crystals (lower ~~plot~~<u>panel</u>). <u>The binwidth is set to the sum of the root-mean-square from table (3) and the errors discussed in section 4.5.</u> In each case, only cases are considered in which the ~~corresponding optical depths is~~ <u>phase fractions are</u> above 0.1 <u>(Liquid water fraction for r_{liq} and ice water fraction for r_{ice}). This results in 4111 of 4590 cases for r_{liq} (89.6%) and 2153 of 4590 cases for r_{ice} (46.9%)</u>.

<u>$IQR_{liq} = 5.9\,\mu$m.</u>

415

5.2 Averaging Kernels <u>and posterior correlation matrices</u>

For all measurements, the mean of the averaging kernels and degrees of freedom are calculated:

$$\mathbf{A} = \begin{pmatrix} 0.77 & 0.48 & -0.17 & -0.02 \\ 0.19 & 0.45 & 0.25 & -0.01 \\ -0.04 & 0.14 & 0.74 & 0.05 \\ -0.03 & -0.1 & 0.29 & 0.3 \end{pmatrix} \tag{15}$$

$$tr(\mathbf{A}) = 2.25 \tag{16}$$

420　This mean averaging kernel matrix contains both single-phase clouds and mixed-phase clouds. Since only two parameters are determined in the single-phase cases, they perturb the mean number of degrees of freedom for all measurements. As seen in the statistics, there are less cases with ice-containing clouds. This ~~also decreases~~ <u>lowers</u> the entries on the diagonals for τ_{ice}

20
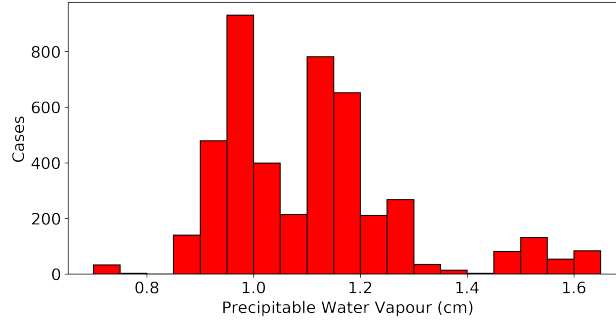
Figure 8. ~~Statistics~~ Histogram of the precipitable water vapour during the measurements of atmospheric radiances.

and r_{ice} as they are 0 in all-liquid clouds. Therefore, the mean averaging kernel was also calculated for all mixed-phase clouds:

$$\mathbf{A}_{mixed-phase} = \begin{pmatrix} 0.62 & 0.22 & -0.35 & -0.03 \\ 0.32 & 0.7 & 0.47 & -0.04 \\ -0.08 & 0.16 & 0.66 & 0.1 \\ -0.14 & -0.07 & 0.17 & 0.59 \end{pmatrix} \tag{17}$$

425 $$tr(\mathbf{A}_{mixed-phase}) = 2.57 \tag{18}$$

~~.~~ The number of degrees of freedom in this case is 2.57. The entries for the effective radii are at the same size as those for the optical depth. ~~However, one has to keep in mind that this averaging kernel has no information about the ice crystal shape. If the assumed shape of ice crystals is inappropriate,~~

The posterior correlation matrix $\mathbf{R}$ gives the correlations of one retrieved parameter to another. For mixed-phase clouds, $\mathbf{R}$ is

430 $$\mathbf{R}_{mixed-phase} = \begin{pmatrix} 1.00 & 0.50 & -0.07 & -0.40 \\ 0.50 & 1.00 & 0.02 & -0.23 \\ -0.07 & 0.02 & 1.00 & 0.13 \\ -0.41 & -0.23 & 0.13 & 1.00 \end{pmatrix} \tag{19}$$

Largest correlation appear between τ_{liq} and τ_{ice} ($|r| = 0.50$), which points to a difficult phase determination. Apart from the correlation of the optical thicknesses, the ~~result might be the correct size for the assumed ice crystal shape, but it is not the real~~ comparatively high correlation between r_{ice} ~~due to different geometries.~~

and τ_{liq} is striking, which suggests that both parameters cannot be determined completely independently of each other.

435 ### 5.3 Precipitable water vapour

A crucial spectral region for the determination of the cloud phase ~~are the spectral windows~~ is the spectral window in the far-infrared between $500\,\mathrm{cm}^{-1}$ and $600\,\mathrm{cm}^{-1}$ (Rathke et al., 2002). This spectral region is sensitive to the concentration of water
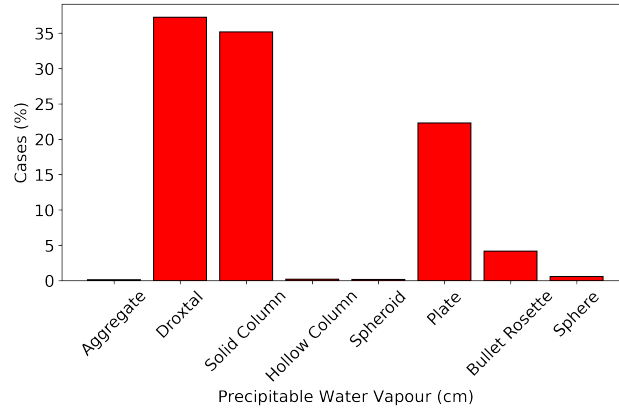
Figure 9. Percentage of retrievals ~~, divided by the chosen~~ for each ice particle shape. Most particles are modelled as droxtals (37 %), solid columns (35 %), plates (22 %) and bullet rosettes (4 %)

Table 6. Results of the comparison between TCWret and Cloudnet. Mean Bias and Root-Mean-Square error refer to the difference of both datasets.

Quantity	$|r|$	Mean Bias	Root-Mean-Square error
LWP	0.65	$2.5\,\mathrm{g\cdot m^{-2}}$	$10.4\,\mathrm{g\cdot m^{-2}}$
$\mathrm{LWP} < 20\,\mathrm{g\cdot m^{-2}}$	0.52	$4.0\,\mathrm{g\cdot m^{-2}}$	$9.5\,\mathrm{g\cdot m^{-2}}$
$\mathrm{LWP}\,(PWV < 1\,\mathrm{cm})$	0.73	$1.1\,\mathrm{g\cdot m^{-2}}$	$8.3\,\mathrm{g\cdot m^{-2}}$
$\mathrm{LWP} < 20\,\mathrm{g\cdot m^{-2}}\,(PWV < 1\,\mathrm{cm})$	0.7	$2.6\,\mathrm{g\cdot m^{-2}}$	$5.9,\mathrm{g\cdot m^{-2}}$
IWP	0.41	$1.5\,\mathrm{g\cdot m^{-2}}$	$16.8\,\mathrm{g\cdot m^{-2}}$
r_{liq}	0.68	$4.5\,\mathrm{\mu m}$	$5.3\,\mathrm{\mu m}$
r_{liq} (maximum)	0.69	$3.1\,\mathrm{\mu m}$	$4.2\,\mathrm{\mu m}$

vapour in the atmosphere. The amount of water vapour is expressed by the precipitable water vapour PWV, which has been calculated from the radiosonde measurements. The far-infrared spectral region becomes nearly ~~intransparent~~ opaque to infrared radiation for PWV $> 1\,\mathrm{cm}$ ~~(Cox et al., 2016)~~(Cox et al., 2015). During the measurement campaign the PWV was greater than $1\,\mathrm{cm}$ in 62 % of the cases. Therefore, the datasets for PWV greater than $1\,\mathrm{cm}$ are not removed from the analysis. Statistics of PWV are shown in figure (8).

440

5.4 Comparison to Cloudnet

To compare result from TCWret and Cloudnet, a combined dataset of TCWret ~~result~~ results is created in the following way: ~~Where r_{ice} is below 30 µm, we used the result with ice crystals~~ Since the shapes of the ice crystals are not known, the retrievals were carried out for all ice crystal shapes. However, this procedure leads to up to 8 results per measurement, so a selection was made. The aim of the following selection is that all ice crystals with $r_{ice} < 30$ µm are modelled as droxtals~~.~~, while larger ice crystals are modelled as either plates, bullet rosettes or solid columns. This choice is motivated by Yang et al. (2007). The accepted result then is determined as follows:

1. If r_{ice} ~~is above~~ for plates, bullet rosettes and solid columns or for droxtals are less than 30 µm, ~~we randomly chose the result retrieved using plates, solid columns or bullet rosette. Figure (9) shows the percentage of the used ice crystal shape in this new dataset. This choice is motivated by the ice crystal shapes described by Yang et al. (2007).~~ the result using ice crystals as droxtals is accepted.

2. If r_{ice} for droxtals are greater than 10 µm, the result that uses plates, bullet rosettes or solid columns is accepted. To choose one of the datasets, a random number is drawn which selects plates in 35%, bullet rosettes in 15% and solid columns in 50%.

3. If none of the conditions apply, the data for which the degrees of freedom of the outcome are highest is accepted.

The first condition ensures that all small ice particles are classified as droxtals, while the second ensures that all larger particles are classified as plates, solid columns or bullet rosettes. Stricter thresholds would more often result in only the last condition applying, which should be avoided as much as possible.

As additional constraint, we only allow results where $r_{liq} < r_{ice}$. This is motivated by the following: The results of r_{liq} and r_{ice} ~~will show ,~~ show that r_{liq} is usually smaller than r_{ice}. ~~From the estimation of the retrieval performance using the testcases ans $\bar{r}$ can be seen, that an underestimated r_{ice} comes with an overestimated r_{liq}~~ This applies to both TCWret and Cloudnet. Therefore, cases with $r_{liq} > r_{ice}$ are likely cases with a too small r_{ice} and a too large r_{liq}. For the comparison between TCWret and Cloudnet, results from both datasets were averaged over a time period of two minutes. This has been done because the underlying measurement systems have different temporal resolutions, also both measurement systems were at different locations on the ship. Cloudnet results do not contain optical depths, but water paths and droplet radii, therefore we will compare LWP and IWP, r_{liq} and r_{ice}. Correlation coefficients, mean biases and root-mean-square errors are shown in table (6).

5.4.1 Ice Water Path and ice effective radius

~~Results of the comparison between TCWret and Cloudnet for ice-related quantities. Mean gives TCWret minus Cloudnet. Quantity |r| p-Value Mean STD IWP 0.41 < 0.05 1.54 g·m^{-2} 16.69 g·m^{-2} IWP ($PWV < 1$ cm) 0.31 < 0.05 1.67 g·m^{-2} 11.55 g·m^{-2} r_{ice} −0.04 > 0.05 −16.77 µm 12.83 µm~~
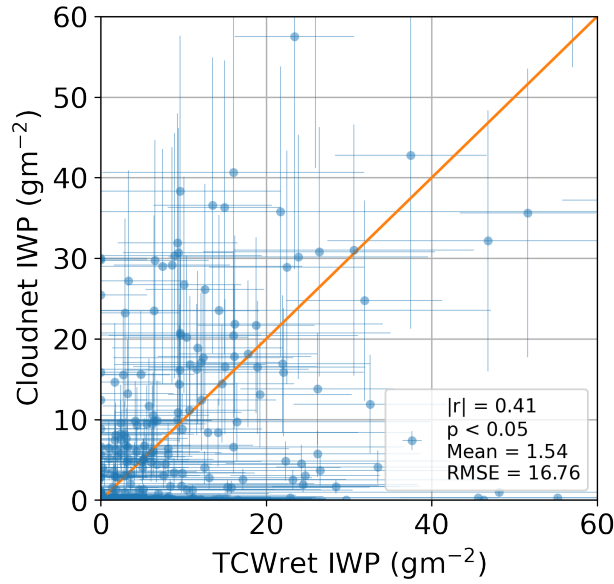
Figure 10. Ice water path of TCWret versus IWP from Cloudnet~~for *PWV* < 1 cm~~.

~~Results for the ice-related quantities are shown in table (??). For~~ Although TCWret can determine r_{ice} ~~, no significant~~
475 ~~correlation between TCWret and Cloudnet could be found . In general,~~ from the simulated spectra, no correlation can be found
between the TCWret and Cloudnet data. From the error considerations in previous sections it was shown that the RMSE for
the simulated spectra is already 10.0 μm. Taking into account uncertainties in the atmospheric data and the calibration, an
additional uncertainty term of 13.1 μm is obtained, so that r_{ice} ~~of TCWret is 16.77 μm smaller than~~ is already subject to high
uncertainties. According to the posterior correlation matrix, r_{ice} ~~from the Cloudnet retrieval. In contrast to the testcases where~~
480 ~~retrieval~~ correlates with τ_{liq}, so that there is no completely independent result of r_{ice} ~~has been proven to be possible, the ice~~
~~crystal geometry in the real measurements does not necessarily agree with the real ice shape. As seen in the study regarding~~
~~the influence of the ice crystal geometry, an inappropriate geometry leads to large uncertainties in the estimation~~ . A better
determination of r_{ice} could be achieved by a better A priori x_a, but the problem remains that according to the averaging kernel
matrix only 2.57 degrees of freedom exist in the measurements.

485

Figure (10) shows the results for the IWP. Although ~~the IWP in TCWret is calculated from r_{ice}, a significant correlation~~
~~between TCWret and Cloudnet can be observed. Withouth limiting the PWV, the~~ a correlation can be found, there is large
spread between the datasets. The difference between TCWret and Cloudnet is ~~$(1.54 \pm 16.69)\,\mathrm{g \cdot m^{-2}}$ and with limiting the~~
~~PWV to values below 1 cm the difference is $(1.67 \pm 11.55)\,\mathrm{g \cdot m^{-2}}$. As the mean IWP in the measurements is $9.92\,\mathrm{g \cdot m^{-2}}$,~~
490 ~~the measurements are~~ $(1.5 \pm 16.8)\,\mathrm{g \cdot m^{-2}}$. The IWP is calculated according to equation (4) from τ_{ice} and r_{ice}, where r_{ice}
influences the IWP of the TCWret data set. Furthermore, the IWP during the measurement campaign is $9.9\,\mathrm{g \cdot m^{-2}}$, very low
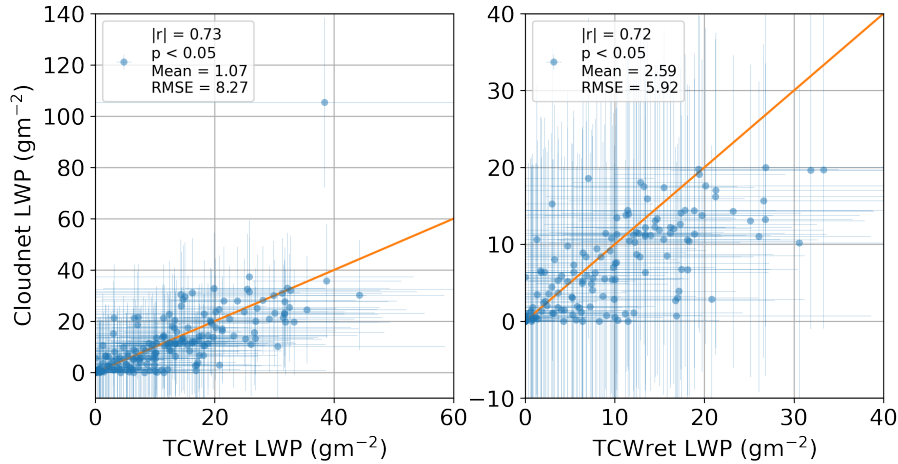
Figure 11. Liquid water path of TCWret versus Cloudnet for $PWV < 1\,\text{cm}$. Left scatter plot contains all measurements, whereas the right plot only shows clouds with LWP $< 20\,\text{g}\cdot\text{m}^{-2}$.

and within the RMSE of TCWret when retrieving the simulated spectra. The IWP is therefore ~~at the lower~~ ~~threshold of the detectable IWP from TCWret. This could be improved by external knowledge of the ice crystal geometry~~ limit of what can be determined with TCWret and is considered as less reliable.

5.4.2 Liquid Water Path and effective droplet radius

~~Results of the comparison between TCWret and Cloudnet for liquid-related quantities. Mean gives TCWret minus Cloudnet.~~
~~Quantity $|r|$ p-Value Mean STDLWP 0.65 < 0.05 2.48 g·m^{-2} 10.13 g·m^{-2}LWP $< 20\,\text{g}\cdot\text{m}^{-2}$ 0.52 < 0.05 3.98 g·m^{-2}~~
~~8.60 g·m^{-2}LWP ($PWV < 1\,\text{cm}$) 0.73 < 0.05 1.07 g·m^{-2} 8.20 g·m^{-2}LWP $< 20\,\text{g}\cdot\text{m}^{-2}$ ($PWV < 1\,\text{cm}$) 0.72 < 0.05 2.59 g·m^{-2}~~
~~5.32 g·m^{-2} r_{liq} 0.66 < 0.05 4.40 μm 2.69 μm r_{liq} ($PWV < 1\,\text{cm}$) 0.47 < 0.05 3.53 μm 2.35 μm~~

~~In table (**??**) the correlation coefficients, means and standard deviations for LWP and r_{liq} are shown. In the case of LWP, for both the data with a limitation of the PWV to 1 cm and without this limitation a significant correlation of the results is observed. Figure (11) (left side) shows~~ Results of liquid water path from TCWret and Cloudnet are correlated. The difference is $2.5\,\text{g}\cdot\text{m}^{-2} \pm 10.4\,\text{g}\cdot\text{m}^{-2}$ with no restriction to the maximum water path. From this we conclude that the LWP from ~~Cloudnet and TCWret for cases with PWV $< 1\,\text{cm}$. The standard deviation of 10.13 g·m^{-2} for all cases and 8.20 g·m^{-2} for the cases with PWV $< 1\,\text{cm}$ is less than~~ the ~~mean error of the LWP from Cloudnet (20.40 g·m^{-2}~~ TCWret-dataset is reliable. As mentioned earlier, a large PWV interferes with the retrieval, as the water vapour has a larger influence on the microwindows. Therefore, we additionally remove all cases from the analysis, where the PWV is larger than 1 cm. This reduces the mean bias to $1.1\,\text{g}\cdot\text{m}^{-2}$ and the RMSE to $8.3\,\text{g}\cdot\text{m}^{-2}$. The results with PWV $< 1\,\text{cm}$ are shown in figure (11, left panel).
~~As seen, the standard deviation of the comparison is lower than those stated by Cloudnet for the individual measurement, so we will show how the results for very thin clouds are. Therefore clouds with LWP $< 20\,\text{g}\cdot\text{m}^{-2}$ retrieved by Cloudnet will be~~
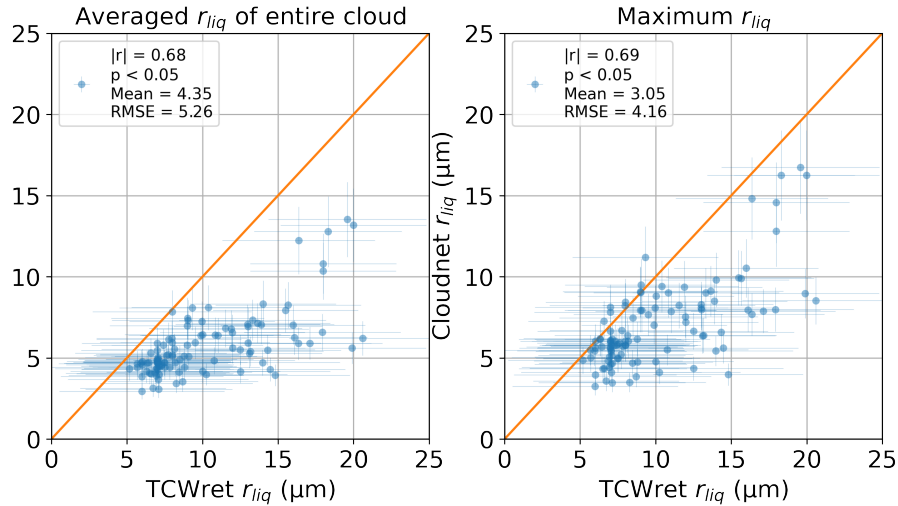
Figure 12. r_{liq} of TCWret versus r_{liq} from Cloudnet averaged over the entire cloud (left panel) and maximum value of the cloud from Cloudnet.

~~compared to LWP from TCWret. These results are~~ Since the LWP of TCWret correlates with that of the Cloudnet product, and since the RMSE of the LWP is far below the uncertainty of ~~Cloudnet, but as the standard deviation of the LWP for all clouds is below $20\,\mathrm{g \cdot m^{-2}}$,~~ the ~~comparison to TCWret allows an assessment of whether the Cloudnet-data is reliable for very thin clouds during this measurement campaign.~~ LWP of the Cloudnet product, we reduced the maximum LWP to investigate

515   whether a correlation can also be observed for clouds with an $LWP < 20\,\mathrm{g \cdot m^{-2}}$. With a real uncertainty of $\pm 20\,\mathrm{g \cdot m^{-2}}$ the correlation is expected to disappear.

Results for very thin clouds (and PWV $< 1\,\mathrm{cm}$) are shown in figure (11) (right side). Again, ~~a signficiant correlation ($|r| = 0.72$) is observed. The standard deviation~~ results are correlated. The RMSE for these clouds is ~~$5.32\,\mathrm{g \cdot m^{-2}}$~~ $5.9\,\mathrm{g \cdot m^{-2}}$ with a mean bias of $2.6\,\mathrm{g \cdot m^{-2}}$. Without any restrictions on the PWV, there is a RMSE of $9.5\,\mathrm{g \cdot m^{-2}}$ and a mean bias of $4.0\,\mathrm{g \cdot m^{-2}}$. From

520   the comparison with TCWret, it can be concluded that during this measurement campaign, Cloudnet's results for thin clouds with LWP $< 20\,\mathrm{g \cdot m^{-2}}$ are also reliable despite the stated error of $20.40\,\mathrm{g \cdot m^{-2}}$.

It should be noted that Cloudnet and TCWret use the atmospheric profiles from the radiosonde measurements carried out on the RV Polarstern. Apart from that, however, both the measuring instruments and the retrievals are different. Furthermore,

525   TCWret does not use information from Cloudnet as A Priori. Since TCWret has also shown comparable agreement with the LWP of the simulated spectra in the test cases (mean bias is $-1.6\,\mathrm{g \cdot m^{-2}}$, RMSE is $6.3\,\mathrm{g \cdot m^{-2}}$), it is to be expected that TCWret and thus also Cloudnet have independently determined the LWP correctly.

Figure (12) shows the results for r_{liq}. The left panel shows the results where r_{liq} of Cloudnet is averaged over the entire cloud. The right panel shows the maximum r_{liq} of the cloud in the Cloudnet data. Only results from TCWret are considered

530   if $f_{ice} < 0.9$. ~~Accordingly, pure ice clouds are ignored~~As in the LWP, a correlation between the data can be observed. Overall, there is an overestimation of the r_{liq} of TCWret by ~~4.40 μm~~ 4.4 μm on average. ~~The standard deviation is 2.79 μm. A high PWV do not worsen the results of the retrieval. While the standard deviation is within the range of what would be expected based on the testcases, the mean deviation is well above that from the testcases. This indicates that TCWret can determine the effective radius within the range of inaccuracies, but that there is a systematic effect that leads to an overestimation compared to~~ If only

535   considering the maximum r_{liq} ~~of Cloudnet . To this end, refer to the mean effective radius $\bar{r} = (1 - f_{ice}) \cdot r_{liq} + f_{ice} \cdot r_{ice}$, which can be well determined by TCWret . In the previous section it was shown that TCWret underestimates r_{ice}.~~ The large in Cloudnet, the mean bias decreases to 3.1 μm. The same applies to the RMSE, which decreases from 5.3 μm to 4.2 μm. These results indicate that r_{liq} ~~observed here is thus consistent with the small r_{ice} compared to Cloudnet: When real larger ice particles are identified as liquid droplets in the retrieval,~~ in TCWret does not take into account the entire cloud, which is to be

540   expected since the r_{liq} ~~increases as r_{ice} decreases. Just like r_{ice},~~ in Cloudnet is determined using the altitude-resolved radar reflectivity, while TCWret uses the radiance of the clouds measured on the ground. However, the observed correlation allows a correction of r_{liq} ~~thus improves if the ice crystal geometry was determined via other measurements~~in TCWret as a function of r_{liq} itself.

6   Data availability

545   For ~~accessability~~ accessibility of used and shown datasets, see table (7).

7   Code availability

The retrieval algorithm TCWret is available at https://doi.org/10.5281/ZENODO.4621127 (Richter, 2021) with external sub-routines at https://doi.org/10.5281/ZENODO.4618142 and https://doi.org/10.5281/ZENODO.4618106. ~~Jupyer-Notebooks~~Jupyter-Noteboo[...] to perform the comparisons to Cloudnet are available at https://github.com/RichterIUP/evaluation_tcwret.

550 ## 8   Summary and Conclusion

~~In this publication, a~~ A dataset of microphysical cloud parameters of optically thin clouds ~~was~~ is presented. The measurements were carried out on the ship RV *Polarstern* in summer 2017 in the Arctic Ocean around Svalbard and in the Fram Strait. Measurements were performed using a mobile FTIR spectrometer, operated in emission mode (EM-FTIR). A calibration of the EM-FTIR was performed with a blackbody radiator, whose temperature was alternately set to $100\,°C$ and ambient temperature.

555   The spectrometer was operated in an air-conditioned container. Radiances between $500\,\mathrm{cm}^{-1}$ and $2000\,\mathrm{cm}^{-1}$ were recorded. The retrieval of cloud parameters ~~was~~ is performed using the Total Cloud Water retrieval (TCWret). TCWret uses the optimal estimation method to invert atmospheric radiances. The radiative transfer model used is LBLDIS, which utilizes optical depths of atmospheric trace gases calculated with LBLRTM and then calculates the spectral radiances using DISORT. Single-scattering parameters for clouds are read from pre-calculated databases. Retrieval products are the optical depths of water and

27

560 ice and the corresponding effective radii. From these products, liquid water path and ice water path are calculated. TCWret also uses profiles of air pressure, humidity and temperature from measurements with Vaisala RS92 radiosondes and information about cloud height from measurements of the ceilometer CL51, which is on board the RV *Polarstern*.

~~Retrieval performance was tested using a dataset of testcases, containing examples of clouds typically observed in the Arctic. Using the correct ice particle shapes, TCWret is able to estimate optical depths, effective radii and water paths for liquid water~~

565 ~~and ice. The comparison with~~ During the measurement campaign, a data set with 5564 retrievals was created. A comparison to the simultaneously performed retrievals of the Cloudnet network on the *Polarstern* shows that:

- The LWP of both data sets are ~~in agreement~~ correlated. From this is concluded, that the retrieved LWP from TCWret is reliable. In addition, it could be shown using the TCWret dataset that during this measurement campaign also the measurement data of thin clouds (LWP $< 20\,\mathrm{g\cdot m^{-2}}$) of the Cloudnet retrieval are reliable despite the given error of
570 $20\,\mathrm{g\cdot m^{-2}}$.

- ~~A significant~~ As well as for the LWP, a correlation for r_{liq} is observed~~, in contrast to r_{ice}. In the testcases r_{ice} could also be determined~~. However, ~~the shape of the ice crystals was known there , in contrast to the ice crystals known during the measurement campaign. The effective radius of the ice crystals in TCWret is too small compared to Cloudnet. This affects r_{liq}, which is overestimated compared to~~ there is a increasing bias with increasing r_{liq}. This can be corrected
575 using the results from Cloudnet.

- ~~The IWP can be determined despite the lack of information about the ice crystal shape. However, the IWP values during the measurement campaign are at the lower limit of what TCWret can determine based on the observed standard deviations.~~ Only a low correlation can be found for the IWP, while r_{ice} does not correlate. Therefore the IWP is considered to be less reliable than the liquid water-products.

580 Despite the difficulty in determining IWP and r_{ice}, this presented data set is useful for downward cloud radiative flux calculations. Since TCWret determines the cloud parameters from the spectral radiance, the calculated cloud parameters are those that match the observed radiance. This is also true if IWP and r_{ice} are affected by errors.

In summary, the dataset of cloud parameters and water paths from TCWret provides a helpful complement to the results of the LWP from Cloudnet, but at the same time benefits from its r_{liq}. Due to the consistent calculation of cloud parameters over
585 the entire cruise, the results from TCWret additionally provide information about clouds during PS107, where only EM-FTIR measurements are available.

Appendix A: Brief description of the Cloudnet synergistic retrieval

The LWP is determined using the HATPRO MWR, which uses two frequency bands between 22.24 GHz and 31.4 GHz and between 51.0 GHz and 58.0 GHz. A statistical retrieval has been set up using radiosonde data from Ny-Alesund, consistent with
590 the procedure described in Löhnert and Crewell (2003) and leading a to a RMSE of $22.4\,\mathrm{g\cdot m^{-2}}$. If a data point was classified as pure liquid, the effective radius of the cloud droplets is determined from the radar reflectivity and the LWP according to

the retrieval of Frisch et al. (2002). The IWC was determined according to Hogan et al. (2006) via an empirical formula from temperature and radar reflectivity. The IWP was determined by vertical integration of the IWC. The calculation of the IWP was carried out specifically for this study. The determination of r_{ice} is done analogously to the IWC from the radar reflectivity and the temperature by an empirical formula (Griesche et al., 2020f).

Appendix B: Description of TCWret

B1 Working principle of TCWret

TCWret retrieves optical depths of liquid water and ice water and the effective radii of liquid water droplets and ice crystals from infrared spectral radiances. The retrieval of microphysical cloud parameters is a nonlinear problem, so an iterative algorithm is needed:

$$\boldsymbol{x}_{n+1} = \boldsymbol{x}_n + \boldsymbol{s}_n \tag{B1}$$

Here $\boldsymbol{x_n}$ and $\boldsymbol{x_{n+1}}$ are the state vectors containing cloud parameters of the n-th and $(n+1)$-th steps and $\boldsymbol{s_n}$ is the modification of the cloud parameters during the n-th iteration. The state vector contains the optical depths and effective radii

$$\boldsymbol{x}_n = \begin{pmatrix} \tau_{liq,n} \\ \tau_{ice,n} \\ r_{liq,n} \\ r_{ice,n} \end{pmatrix} \tag{B2}$$

The governing equation to determine $\boldsymbol{s}_n$ is

$$\left(\mathbf{K}_n^T \mathbf{S_y}^{-1} \mathbf{K}_n + \mathbf{S_a}^{-1} + \mu^2 \mathbf{S_a}^{-1} \right) \boldsymbol{s}_n = \mathbf{K}_n^T \mathbf{S_y}^{-1} \left[\boldsymbol{y} - F(\boldsymbol{x}_n) \right] + \mathbf{S_a}^{-1} \cdot (\boldsymbol{x_a} - \boldsymbol{x}_n) \tag{B3}$$

The quantities in the equation are the jacobian matrix $\mathbf{K} = \left(\frac{\partial F(x_i)_j}{\partial x_i} \right)$, the inverse of the variance-covariance matrix $\mathbf{S_y}^{-1}$, the a priori $\boldsymbol{x_a}$ of the cloud parameters and the inverse covariance matrix of the a priori $\mathbf{S_a}^{-1}$, the measured spectral radiances $\boldsymbol{y}$, the calculated spectral radiances $F(\boldsymbol{x_n})$ and the Levenberg-Marquardt term $\mu^2 \cdot \mathbf{S_a}^{-1}$.
The aim of the iterations is to minimize the cost function $\xi^2(\boldsymbol{x})$.

$$\xi^2(\boldsymbol{x}_n) = \left[\boldsymbol{y} - F(\boldsymbol{x}_n) \right]^T \mathbf{S_y}^{-1} \left[\boldsymbol{y} - F(\boldsymbol{x}_n) \right] + \left[\boldsymbol{x_a} - \boldsymbol{x}_n \right]^T \mathbf{S_a}^{-1} \left[\boldsymbol{x_a} - \boldsymbol{x}_n \right] \tag{B4}$$

Convergence is reached, if the change of the cost function is below a given threshold, here set to 0.1%:

$$\frac{\xi^2(x_{n+1}) - \xi^2(x_n)}{\xi^2(x_{n+1})} < 0.001 \tag{B5}$$

However, convergence in the sense of the cost function does not necessarily mean that the fitted and measured spectrum match. For example, the step size parameter of the Levenberg-Marquardt method could be so large that the cost function changes

little. Then the convergence criterion is fulfilled, but the fit does not agree with the measurement. To identify these cases, a reduced-χ^2-test is performed. This test is used to calculate the distance between calculated and measured radiance, taking into account the variance of the spectrum σ^2. It is defined as

$$\chi^2_{reduced} = \frac{1}{DOF} \cdot \sum_{m=1}^{N} \frac{y(\bar{\nu}_m) - F(\mathbf{x}, \bar{\nu}_m)}{\sigma^2} \tag{B6}$$

620 with $DOF = $ number of datapoints - number of parameters. The microwindow is denoted as $\bar{\nu}_m$. As empirical values, we assume that all retrievals with $\xi^2_{reduced} < 1.0$ converged correctly. Results with $\tau_{liq} + \tau_{ice} > 6$ are excluded.

As we do not necessarily have prior information about the optical depths and effective radii, we decided to set the covariance of the a priori to large values. This shall ensure that the chosen a priori does not constrain the retrieval too strong. Initial values and a priori are set to equal values: $\mathbf{x_a} = (0.25, 0.25, \log(5.0), \log(20.0))$. The logarithm was chosen so that all entries of $\mathbf{x_a}$

625 have similar size. The variance-covariance matrix of the a priori is set to

$$\mathbf{S_a}^{-1} = \begin{pmatrix} 0.04 & 0 & 0 & 0 \\ 0 & 0.04 & 0 & 0 \\ 0 & 0 & 0.047 & 0 \\ 0 & 0 & 0 & 0.047 \end{pmatrix} \tag{B7}$$

The values in $\mathbf{x_a}$ and $\mathbf{S_a}^{-1}$ are chosen empirically. Since initially no information about the cloud parameters is available, $\mathbf{x_a}$ and $\mathbf{S_a}^{-1}$ should not restrict the retrieval too much. Therefore, the variances in $\mathbf{S_a}^{-1}$ are set to large values.

Variances in $\mathbf{S_y}^{-1}$ are calculated from the spectral region between $1925\,\mathrm{cm}^{-1}$ and $2000\,\mathrm{cm}^{-1}$, where no signal from the

630 atmosphere is expected. The variance-covariance matrix is assumed to be diagonal: $\mathbf{S_y} = \sigma^2 \mathbf{I}$. It is assumed to be the variance of the scene. To retrieve cloud parameters, only radiance from spectral intervals given in table (B1) is used. The variances of $\mathbf{S_y}$ propagated into the covariance matrix $\mathbf{S_r}$ of the result by applying a *transfer matrix* $\mathbf{T}$. In each step $\mathbf{T}$ is calculated taking into account the current step size parameter μ by

$$\begin{cases} \mathbf{T_0} = \mathbf{0} \\ \mathbf{T}_{i+1} = \mathbf{G}_i + \left(\mathbf{I} - \mathbf{G}_i \mathbf{K}_i - \mathbf{M}_i \mathbf{S}_a^{-1} \right) \mathbf{T}_i \end{cases} \tag{B8}$$

635 with $\mathbf{0}$ as zero matrix and $\mathbf{I}$ as identity matrix. $\mathbf{M}_i$ is the inverse of the term in the brackets on the left side of (B3) and $\mathbf{G}_i = \mathbf{M}_i \mathbf{K}_i^T \mathbf{S}_y^{-1}$. Diagonal elements of $\mathbf{S}_r$ are the variances of the final cloud parameters.

Appendix C: Retrieval performance on simulated spectra

A set of simulated testcases containing spectral radiances of artificial clouds with known cloud parameters, created by Cox et al. (2016)

640 , will be used to test the ability of TCWret to retrieve $\tau_{liq}, \tau_{ice}, r_{liq}$ and r_{ice}. Additionally, the derived quantities LWP and

IWP are discussed. This dataset contains several representative cases of Arctic clouds. Clouds are set to be either vertically homogeneous, topped by a layer of liquid water or with thin boundaries. Ice crystal shapes are mostly set to be spheres, but some cases where calculated with hollow columns, solid columns, bullet rosettes or plates. All spectra are convoluted with a sinc-function to the resolution of the IFS 55 Equinox $(0.3\,\mathrm{cm}^{-1})$ and perturbed by a Gaussian distributed noise of

645 $1\,\mathrm{mW}\cdot(\mathrm{sr}\cdot\mathrm{cm}^{-1}\cdot\mathrm{m}^{-2})^{-1}$: We modified the spectral radiance at each wavenumber by drawing a random number from a normal distribution with the true spectral radiance as mean of the distribution and $1\,\mathrm{mW}\cdot(\mathrm{sr}\cdot\mathrm{cm}^{-1}\cdot\mathrm{m}^{-2})^{-1}$ as its standard deviation. This value has been chosen, because it is near the observed standard deviation of the real spectra from the measurement campaign of $0.82\,\mathrm{mW}\cdot(\mathrm{sr}\cdot\mathrm{cm}^{-1}\cdot\mathrm{m}^{-2})^{-1}$. Ice crystals are chosen to be spheres, thus only the testcases which are calculated with spherical ice crystals are used here. The influence of the chosen ice particle form will be adressed later.

650 Table (3) gives the correlation coefficients, mean biases and standard deviations between the retrieved cloud parameters of the testcases and the true cloud parameters. Additionally, the standard deviations calculated via the variance-covariance matrix is given. TCWret is able to determine optical depths and effective radii of the simulated spectra.

Of all direct retrieval products, the optical depths τ_{liq} and τ_{ice} have the highest agreement to the true cloud parameters. For the liquid phase, the difference to the true optical depths is (-0.1 ± 0.5). For the optical depth of the ice phase, the difference

655 is larger with (0.2 ± 0.6). Since τ_{liq} and τ_{ice} include both optical depths and phase, the optical depth of the condensed water $\tau_{cw}=\tau_{liq}+\tau_{ice}$ as well as the fraction of ice in the optical depth $f_{ice}=\tau_{ice}\cdot\tau_{cw}^{(-1)}$ are calculated. Here it becomes clear that the optical depth can be determined accurately $(|r|=0.99$, mean bias and RMSE $(0.1\pm0.2))$. It then also follows that the deviations of τ_{liq} and τ_{ice} come from the phase determination. The deviation for the phase is (0.1 ± 0.3) with a correlation coefficient of $|r|=0.70$.

660 When considering the effective radii, only results of r_{liq} were used in where f_{ice} is less than 0.9. For r_{ice} only results with $f_{ice}>0.1$ are considered. The mean difference of the retrieval from the true parameters and the root-mean-square error are (-2.4 ± 4.1) for r_{liq} and (3.0 ± 10.0) for r_{ice}.

To estimate the influence of the A priori on the calculated result, the Averaging Kernel Matrix is used. The mean averaging kernel matrix over all retrievals is

665
$$\mathbf{A}=\begin{pmatrix} 0.87 & 0.09 & -0.15 & -0.09 \\ 0.11 & 0.90 & 0.19 & 0.03 \\ -0.04 & 0.07 & 0.50 & 0.05 \\ -0.16 & 0.05 & 0.03 & 0.42 \end{pmatrix} \tag{C1}$$

From equation (8) can be seen that the diagonal elements show for each parameter how strong the retrieved parameter is influenced by the a priori. Whereas the diagonal elements of the optical depths are near 1, indicating independence from the a priori, results for r_{liq} and r_{ice} show a larger influence from the a priori. From the trace of the averaging kernels follow 2.69 degrees of freedom of the signal.

670 The water paths are calculated from the optical depths and effective radii, therefore both quantities are influenced by the phase determination, as seen before in $\tau_{liq,ice}$ and $r_{liq,ice}$. The difference from the testcases is (-1.6 ± 6.3) for the LWP and

(1.9 ± 10.0) for the IWP. However, the RMSE for the LWP is less than the minimum RMSE observed for LWP from microwave radiometer of at least $15\,\mathrm{g} \cdot \mathrm{m}^{-2}$ (Löhnert and Crewell, 2003).

Standard devations given by the variance-covariance matrix of the retrieval are shown in table (3) and named as ERR(OE).
675   ERR(OE) is below RMSE for $\tau_{liq,ice}$, $r_{liq,ice}$, LWP and IWP. This might be due to uncertainties from the forward model - which are neglected here - propagated into the retrievals or due to the assumption of a diagonal variance matrix $\mathbf{S_y}$. To compensate these effects, the uncertainties from the posterior covariance matrix are scaled by RMSE/ERR(OE) with the RMSE from table (3) for the discussion in section 6.

C1   Mean Bias and RMSE of effective radii

680   In the previous section, the results for r_{liq} and r_{ice} were only considered for a certain range of f_{ice}. Thus, liquid drops were only included in the consideration if the ice content was not higher than 90%. For ice crystals, the limit was at least 10% ice content. In the following, these limits are shifted so that the results go in the direction of a single-phase retrieval for liquid water and ice.

Table (C1) shows the results for liquid water. The entries at the top describe cases with a higher proportion of liquid water
685   than the cases at the bottom, which allow a higher proportion of ice. They are cumulative, which means that each record also contains the data of the record above it. From the testcases it follows that the RMSE becomes lower the fewer ice crystals are present. Also, the absolute mean bias decreases with lower ice content up to an ice content between 10% and 30%. These results indicate that the presence of ice crystals lead to an underestimation of r_{liq} by TCWret.

Table (C2) show the results for ice crystals. Here we introduced f_{liq}, which is defined as $f_{liq} = 1 - f_{ice}$ to create a table
690   consistent with table (C1). Here one can see that the RMSE of r_{ice} is almost independent of the water content. However, there is a dependence of the mean bias on water content. While removing clouds with very high water content leads to a decrease in absolute mean bias, the absolute value of mean bias increases for clouds with high ice content, so that TCWret underestimates r_{ice} of the simulated spectra.

Appendix D: Influence of trace gas concentrations on the retrieval

695   In LBLRTM, a standard atmosphere was used for gases except water vapour. Therefore, the concentration of CO_2 is set to $330\,\mathrm{ppm}$, although the real concentration in summer 2017 is about $410\,\mathrm{ppm}$. To investigate the influence of an incorrect trace gas concentration, retrievals from the 11th June 2016 have been performed with both atmospheric concentrations of CO_2. Differences are calculated for the cloud parameters τ_{liq}, τ_{ice}, r_{liq} and r_{ice} and shown in figure (D1). For all parameters, correlation coefficients between $|r| = 0.98$ and $|r| = 1.00$ can be observed. The maximum mean bias is observed for r_{liq}
700    $(0.1\,\mathrm{\mu m})$ and the maximum RMSE is observed for r_{ice} $(1.3\,\mathrm{\mu m})$. From this it can be concluded that the influence of the trace gas concentration is negligible compared to the other uncertainties.
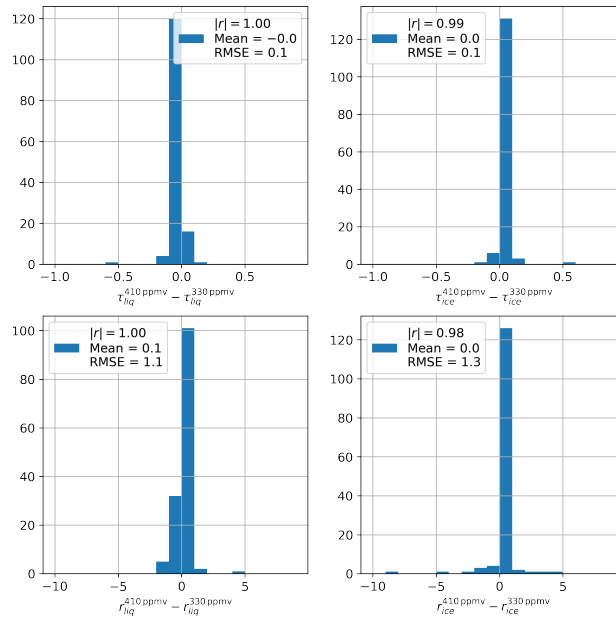
Figure D1. Histograms of differences for CO_2 concentrations of $410\,\mathrm{ppm}$ and $330\,\mathrm{ppm}$ for τ_{liq}, τ_{ice}, r_{liq} and r_{ice}.

Appendix E: Ice crystal shapes in the netCDF-file

Table (E1) refers to each key in the field *ice_shape* in the netCDF-file the corresponding ice crystal shape.

References

Becker, E. and Notholt, J.: Intercomparison and validation of FTIR measurements with the Sun, the Moon and emission in the Arctic, Journal of Quantitative Spectroscopy and Radiative Transfer, 65, 779 – 786, https://doi.org/https://doi.org/10.1016/S0022-4073(99)00154-5, http://www.sciencedirect.com/science/article/pii/S0022407399001545, 2000.

Becker, E., Notholt, J., and Herber, A.: Tropospheric aerosol measurements in the Arctic by FTIR-emission and star photometer extinction spectroscopy, Geophysical Research Letters, 26, 1711–1714, https://doi.org/10.1029/1999GL900336, https://agupubs.onlinelibrary.wiley.com/doi/abs/10.1029/1999GL900336, 1999.

Ceccherini, S. and Ridolfi, M.: Technical Note: Variance-covariance matrix and averaging kernels for the Levenberg-Marquardt solution of the retrieval of atmospheric vertical profiles, Atmospheric Chemistry and Physics, pp. 3131 – 3139, 2010.

Clough, S. A., Shephard, M. W., Mlawer, E. J., Delamere, J. S., Iacono, M. J., Cady-Pereira, K., Boukabara, S., and Brown, P. D.: Atmospheric radiative transfer modeling: a summary of the AER codes, Journal of Quantitative Spectroscopy & Radiative Transfer, 91, 233 – 244, 2005.

Cox, C. J., Walden, V. P., Rowe, P. M., and Shupe, M. D.: Humidity trends imply increased sensitivity to clouds in a warming Arctic, Nature Communications, 6, https://doi.org/10.1038/ncomms10117, 2015.

Cox, C. J., Rowe, P. M., Neshyba, S. P., and Walden, V. P.: A synthetic data set of high-spectral-resolution infrared spectra for the Arctic atmosphere, Earth System Science Data, 8, 199–211, https://doi.org/10.5194/essd-8-199-2016, https://www.earth-syst-sci-data.net/8/199/2016/, 2016.

Downing, H. D. and Williams, D.: Optical constants of water in the infrared, Journal of Geophysical Research (1896-1977), 80, 1656–1661, https://doi.org/10.1029/JC080i012p01656, https://agupubs.onlinelibrary.wiley.com/doi/abs/10.1029/JC080i012p01656, 1975.

Frisch, S., Shupe, M., Djalalova, I., Feingold, G., and Poellot, M.: The Retrieval of Stratus Cloud Droplet Effective Radius with Cloud Radars, Journal of Atmospheric and Oceanic Technology, 19, 835 – 842, https://doi.org/10.1175/1520-0426(2002)019<0835:TROSCD>2.0.CO;2, https://journals.ametsoc.org/view/journals/atot/19/6/1520-0426_2002_019_0835_troscd_2_0_co_2.xml, 2002.

Griesche, H., Seifert, P., Engelmann, R., Radenz, M., and Bühl, J.: OCEANET-ATMOSPHERE Microwave Radiometer HATPRO during PS106, https://doi.org/10.1594/PANGAEA.919359, https://doi.pangaea.de/10.1594/PANGAEA.919359, 2020a.

Griesche, H., Seifert, P., Engelmann, R., Radenz, M., and Bühl, J.: Cloudnet IWC during PS106, https://doi.org/10.1594/PANGAEA.919452, https://doi.pangaea.de/10.1594/PANGAEA.919452, 2020b.

Griesche, H., Seifert, P., Engelmann, R., Radenz, M., and Bühl, J.: Cloudnet ice particles effective radius during PS106, https://doi.org/10.1594/PANGAEA.919386, https://doi.org/10.1594/PANGAEA.919386, 2020c.

Griesche, H., Seifert, P., Engelmann, R., Radenz, M., and Bühl, J.: Cloudnet LWC during PS106, https://doi.org/10.1594/PANGAEA.919383, https://doi.org/10.1594/PANGAEA.919383, 2020d.

Griesche, H., Seifert, P., Engelmann, R., Radenz, M., and Bühl, J.: Cloudnet liquid droplet effective radius during PS106, https://doi.org/10.1594/PANGAEA.919399, https://doi.org/10.1594/PANGAEA.919399, 2020e.

Griesche, H. J., Seifert, P., Ansmann, A., Baars, H., Barrientos Velasco, C., Bühl, J., Engelmann, R., Radenz, M., Zhenping, Y., and Macke, A.: Application of the shipborne remote sensing supersite OCEANET for profiling of Arctic aerosols and clouds during *Polarstern* cruise PS106, Atmospheric Measurement Techniques, 13, 5335–5358, https://doi.org/10.5194/amt-13-5335-2020, https://amt.copernicus.org/articles/13/5335/2020/, 2020f.

750   Hersbach, H., Bell, B., Berrisford, P., Biavati, G., Horányi, A., Muñoz Sabater, J., Nicolas, J., Peubey, C., Radu, R., Rozum, I., Schepers, D., Simmons, A., Soci, C., Dee, D., and Thépaut, J.-N.: ERA5 hourly data on pressure levels from 1979 to present. Copernicus Climate Change Service (C3S) Climate Data Store (CDS). (Accessed on 25-Sep-2020), https://doi.org/10.24381/cds.bd0915c6, 2018.

Hogan, R. J., Mittermaier, M. P., and Illingworth, A. J.: The Retrieval of Ice Water Content from Radar Reflectivity Factor and Temperature and Its Use in Evaluating a Mesoscale Model, Journal of Applied Meteorology and Climatology, 45, 301 – 317,

755   https://doi.org/10.1175/JAM2340.1, https://journals.ametsoc.org/view/journals/apme/45/2/jam2340.1.xml, 2006.

Illingworth, A. J., Hogan, R. J., O'Connor, E., Bouniol, D., Brooks, M. E., Delanoé, J., Donovan, D. P., Eastment, J. D., Gaussiat, N., Goddard, J. W. F., Haeffelin, M., Baltink, H. K., Krasnov, O. A., Pelon, J., Piriou, J.-M., Protat, A., Russchenberg, H. W. J., Seifert, A., Tompkins, A. M., van Zadelhoff, G.-J., Vinit, F., Willén, U., Wilson, D. R., and Wrench, C. L.: Cloudnet, Bulletin of the American Meteorological Society, 88, 883–898, https://doi.org/10.1175/BAMS-88-6-883, 2007.

760   Knuteson, R. O., Revercomb, H. E., Best, F. A., Ciganovich, N. C., Dedecker, R. G., Dirckx, T. P., Ellington, S. C., Feltz, W. F., Garcia, R. K., Howell, H. B., Smith, W. L., Short, J. F., and Tobin, D. C.: Atmospheric Emitted Radiance Interferometer. Part II: Instrument Performance, Journal of Atmospheric and Oceanic Technology, 21, 1777–1789, https://doi.org/10.1175/JTECH-1663.1, 2004a.

Knuteson, R. O., Revercomb, H. E., Best, F. A., Ciganovich, N. C., Dedecker, R. G., Dirkx, T. P., Ellington, S. C., Feltz, W. F., Garcia, R. K., Howell, H. B., Smith, W. L., Short, J. F., and Tobin, D. C.: Atmospheric Emitted Radiance Interferometer. Part I: Instrument Design,

765   Journal of Atmospheric and Oceanic Technology, 21, 1763 – 1776, https://doi.org/10.1175/JTECH-1662.1, https://journals.ametsoc.org/view/journals/atot/21/12/jtech-1662_1.xml, 2004b.

Löhnert, U. and Crewell, S.: Accuracy of cloud liquid water path from ground-based microwave radiometry 1. Dependency on cloud model statistics, Radio Science, 38, https://doi.org/https://doi.org/10.1029/2002RS002654, https://agupubs.onlinelibrary.wiley.com/doi/abs/10.1029/2002RS002654, 2003.

770   Macke, A. and Flores, H.: The Expeditions PS106/1 and 2 of the Research Vessel POLARSTERN to the Arctic Ocean in 2017, https://doi.org/10.2312/BzPM_0719_2018, 2018.

Rathke, C. and Fischer, J.: Retrieval of Cloud Microphysical Properties from Thermal Infrared Observations by a Fast Iterative Radiance Fitting Method, Journal of atmospheric and oceanic technology, 17, 1509 – 1524, https://doi.org/10.1175/1520-0426(2000)017<1509:ROCMPF>2.0.CO;2, 2000.

775   Rathke, C., Fischer, J., Neshyba, S., and Shupe, M.: Improving IR cloud phase determination with 20 microns spectral observations, Geophysical Research Letters, pp. 51 – 54, https://doi.org/10.1029/2001GL014594, 2002.

Revercomb, H. E., Buijs, H., Howell, H. B., Laporte, D. D., Smith, W. L., and Sromovsky, L. A.: Radiometric calibration of IR Fourier transform spectrometers: solution to a problem with the High-Resolution Interferometer Sounder, Applied Optics, 27, 3210 – 3218, https://doi.org/10.1364/AO.27.003210, 1988.

780   Richter, P.: Total Cloud Water retrieval, https://doi.org/10.5281/zenodo.4621127, https://doi.org/10.5281/zenodo.4621127, 2021.

Richter, P., Palm, M., Weinzierl, C., and Notholt, J.: Microphysical Cloud Parameters and water paths retrieved from EM-FTIR spectra, measured during PS106 and PS107 in Arctic summer 2017, https://doi.pangaea.de/10.1594/PANGAEA.933829, 2021.

Rodgers, C.: Inverse Methods for Atmospheric Sounding: Theory and Practice, World Scientific, https://doi.org/10.1142/3171, 2000.

Rowe, P. M., Neshyba, S., and Walden, V. P.: Radiative consequences of low-temperature infrared refractive indices for super-

785   cooled water clouds, Atmospheric Chemistry and Physics, 13, 11 925–11 933, https://doi.org/10.5194/acp-13-11925-2013, https://www.atmos-chem-phys.net/13/11925/2013/, 2013.

Rowe, P. M., Cox, C. J., Neshyba, S., and Walden, V. P.: Toward autonomous surface-based infrared remote sensing of polar clouds: retrievals of cloud optical and microphysical properties, Atmospheric Measurement Techniques, 12, 5071–5086, https://doi.org/10.5194/amt-12-5071-2019, https://www.atmos-meas-tech.net/12/5071/2019/, 2019.

790 Schewe, I.: The Expedition PS107 of the Research Vessel POLARSTERN to the Fram Strait and the AWI-HAUSGARTEN in 2017, https://doi.org/10.2312/BzPM_0717_2018, 2018.

Schmithüsen, H.: Ceilometer CL51 raw data measured during POLARSTERN cruise PS106.1, links to files, https://doi.org/10.1594/PANGAEA.883320, https://doi.org/10.1594/PANGAEA.883320, 2017a.

Schmithüsen, H.: Ceilometer CL51 raw data measured during POLARSTERN cruise PS106.2, links to files, 795 https://doi.org/10.1594/PANGAEA.883322, https://doi.org/10.1594/PANGAEA.883322, 2017b.

Schmithüsen, H.: Ceilometer CL51 raw data measured during POLARSTERN cruise PS107, links to files, https://doi.org/10.1594/PANGAEA.883323, https://doi.org/10.1594/PANGAEA.883323, 2017c.

Schmithüsen, H.: Upper air soundings during POLARSTERN cruise PS106.1 (ARK-XXXI/1.1), https://doi.org/10.1594/PANGAEA.882736, https://doi.org/10.1594/PANGAEA.882736, 2017d.

800 Schmithüsen, H.: Upper air soundings during POLARSTERN cruise PS106.2 (ARK-XXXI/1.2), https://doi.org/10.1594/PANGAEA.882843, https://doi.org/10.1594/PANGAEA.882843, 2017e.

Schmithüsen, H.: Upper air soundings during POLARSTERN cruise PS107 (ARK-XXXI/2), https://doi.org/10.1594/PANGAEA.882889, https://doi.org/10.1594/PANGAEA.882889, 2017f.

Shupe, M. and Intrieri, J.: Cloud Radiative Forcing of the Arctic Surface: The Influence of Cloud Properties, Surface Albedo, and Solar 805 Zenith Angle, Journal of Climate, 17, 616 – 628, https://doi.org/10.1175/1520-0442(2004)017<0616:CRFOTA>2.0.CO;2, 2004.

Stamnes, K., Tsay, S. C., Wiscombe, W., and Jayaweera, K.: Numerically stable algorithm for discrete-ordinate-method radiative transfer in multiple scattering and emitting layered media, Applied Optics, 27, 2502 – 2509, 1988.

Turner, D. D.: Arctic Mixed-Phase Cloud Properties from AERI Lidar Observations: Algorithm and Results from SHEBA, Americal Meteorological Society, pp. 427 – 444, 2005.

810 Turner, D. D.: Additional Information for LBLDIS, https://www.nssl.noaa.gov/users/dturner/public_html/lbldis/index.html, 2014.

Turner, D. D., Vogelmann, A. M., Baum, B. A., Revercomb, H. E., and P., Y.: Cloud Phase Determination Using Ground-Based AERI Observations at SHEBA, Americal Meteorological Society, pp. 701 – 715, 2003.

Turner, D. D., Vogelmann, A. M., Austin, R. T., Barnard, J. C., Cady-Pereira, K., Chiu, J. C., Clough, S. A., Flynn, C., Khaiyer, M. M., Liljegren, J., Johnson, K., Lin, B., Long, C., Marshak, A., Matrosov, S. Y., McFarlane, S. A., Miller, M., Min, Q., Minnis, P., O'Hirok, 815 W., Wang, Z., and Wiscombe, W.: Thin Liquid Water Clouds - Their Importance and Our Challenge, Americal Meteorological Society, pp. 177 – 190, https://doi.org/10.1175/BAMS-88-2-I77, 2007.

Warren, S. G.: Optical constants of ice from the ultraviolet to the microwave, Appl. Opt., 23, 1206–1225, https://doi.org/10.1364/AO.23.001206, http://ao.osa.org/abstract.cfm?URI=ao-23-8-1206, 1984.

Wendisch, M., Macke, A., Ehrlich, A., Lüpkes, C., Mech, M., Chechin, D., Dethloff, K., Velasco, C. B., Bozem, H., Brückner, M., Clemen, 820 H.-C., Crewell, S., Donth, T., Dupuy, R., Ebell, K., Egerer, U., Engelmann, R., Engler, C., Eppers, O., Gehrmann, M., Gong, X., Gottschalk, M., Gourbeyre, C., Griesche, H., Hartmann, J., Hartmann, M., Heinold, B., Herber, A., Herrmann, H., Heygster, G., Hoor, P., Jafariserajehlou, S., Jäkel, E., Järvinen, E., Jourdan, O., Kästner, U., Kecorius, S., Knudsen, E. M., Köllner, F., Kretzschmar, J., Lelli, L., Leroy, D., Maturilli, M., Mei, L., Mertes, S., Mioche, G., Neuber, R., Nicolaus, M., Nomokonova, T., Notholt, J., Palm, M., van Pinxteren, M., Quaas, J., Richter, P., Ruiz-Donoso, E., Schäfer, M., Schmieder, K., Schnaiter, M., Schneider, J., Schwarzenböck, A., Seifert, P.,

825   Shupe, M. D., Siebert, H., Spreen, G., Stapf, J., Stratmann, F., Vogl, T., Welti, A., Wex, H., Wiedensohler, A., Zanatta, M., and Zeppenfeld, S.: The Arctic Cloud Puzzle: Using ACLOUD/PASCAL Multiplatform Observations to Unravel the Role of Clouds and Aerosol Particles in Arctic Amplification, Bulletin of the American Meteorological Society, 100, 841–871, https://doi.org/10.1175/BAMS-D-18-0072.1, https://doi.org/10.1175/BAMS-D-18-0072.1, 2019.

Yang, P., Gao, B.-C., Baum, B. A., Hu, Y. X., Wiscombe, W. J., Tsay, S.-C., Winker, D. M., and Nasiri, S. L.: Radiative properties
830   of cirrus clouds in the infrared (8–13um) spectral region, Journal of Quantitative Spectroscopy and Radiative Transfer, 70, 473–504, https://doi.org/https://doi.org/10.1016/S0022-4073(01)00024-3,   https://www.sciencedirect.com/science/article/pii/S0022407301000243, light Scattering by Non-Spherical Particles, 2001.

Yang, P., Zhang, L., Hong, G., Nasiri, S. L., Baum, B. A., Huang, H., King, M. D., and Platnick, S.: Differences Between Collection 4 and 5 MODIS Ice Cloud Optical/Microphysical Products and Their Impact on Radiative Forcing Simulations, IEEE Transactions on Geoscience
835   and Remote Sensing, 45, 2886–2899, https://doi.org/10.1109/TGRS.2007.898276, 2007.

Zasetsky, A. Y., Khalizov, A. F., Earle, M. E., and Sloan, J. J.: Frequency Dependend Complex Refractive Indices of Super-cooled Liquid Water and Ice Determined from Aerosol Extinction Spectra, Journal of Physical Chemistry A, pp. 2760 – 2764, https://doi.org/10.1021/jp044823c, 2005.

Table 7. Datasets used in this publication.

Description	DOI	Citation
Microphysical Cloud Parameters from TCWret	https://doi.pangaea.de/10.1594/PANGAEA.933829	Richter et al. (2021)
OCEANET-ATMOSPHERE Microwave Radiometer HATPRO during PS106	https://doi.org/10.1594/PANGAEA.919359	Griesche et al. (2020a)
Cloudnet IWC during PS106	https://doi.org/10.1594/PANGAEA.919452	Griesche et al. (2020b)
Cloudnet r_{ice} during PS106	https://doi.org/10.1594/PANGAEA.919386	Griesche et al. (2020c)
Cloudnet LWC during PS106	https://doi.org/10.1594/PANGAEA.919383	Griesche et al. (2020d)
Cloudnet r_{liq} during PS106	https://doi.org/10.1594/PANGAEA.919399	Griesche et al. (2020e)
Ceilometer CL51 raw data measured during POLARSTERN cruise PS106.1	https://doi.org/10.1594/PANGAEA.883320	Schmithüsen (2017a)
Ceilometer CL51 raw data measured during POLARSTERN cruise PS106.2	https://doi.org/10.1594/PANGAEA.883322	Schmithüsen (2017b)
Ceilometer CL51 raw data measured during POLARSTERN cruise PS107	https://doi.org/10.1594/PANGAEA.883323	Schmithüsen (2017c)
Upper air soundings during POLARSTERN cruise PS106.1 (ARK-XXXI/1.1)	https://doi.org/10.1594/PANGAEA.882736	Schmithüsen (2017d)
Upper air soundings during POLARSTERN cruise PS106.2 (ARK-XXXI/1.2)	https://doi.org/10.1594/PANGAEA.882743	Schmithüsen (2017e)
Upper air soundings during POLARSTERN cruise PS107 (ARK-XXXI/2)	https://doi.org/10.1594/PANGAEA.882789	Schmithüsen (2017f)

Table B1. Microwindows used in TCWret to retrieve the microphysical cloud parameters of this dataset.

Interval (cm^{-1})
$558.5 - 562.0$
$571.0 - 574.0$
$785.9 - 790.7$
$809.5 - 813.5$
$815.3 - 824.4$
$828.3 - 834.6$
$842.8 - 848.1$
$860.1 - 864.0$
$872.2 - 877.5$
$891.9 - 895.8$
$898.2 - 905.4$
$929.6 - 939.7$
$959.9 - 964.3$
$985.0 - 991.5$
$1092.2 - 1098.1$
$1113.3 - 1116.6$
$1124.4 - 1132.6$
$1142.2 - 1148.0$
$1155.2 - 1163.4$

Table C1. Determination of r_{liq} depending on the cloud phase.

Maximum f_{ice}	$|r|$	Mean Bias	RMSE	Datapoints
0.1	0.97	0.6 µm	2.1 µm	19
0.3	0.90	−0.2 µm	2.3 µm	38
0.5	0.79	−1.0 µm	2.7 µm	87
0.7	0.70	−1.6 µm	3.2 µm	151
0.9	0.59	−2.4 µm	4.1 µm	192

Table C2. Determination of r_{ice} depending on the cloud phase.

Maximum f_{liq}	$|r|$	Mean Bias	RMSE	Datapoints
0.1	0.61	−5.0 µm	12.0 µm	31
0.3	0.59	−0.3 µm	12.0 µm	80
0.5	0.67	1.3 µm	10.2 µm	141
0.7	0.65	2.6 µm	10.2 µm	180
0.9	0.65	2.9 µm	10.1 µm	193

Table E1. Ice crystal shapes in the netCDF-file and the corresponding number

Key	Shape
0	Aggregates
1	Droxtals
2	Solid Columns
3	Hollow Columns
4	Spheroids
5	Plates
6	Bullet Rosettes
7	Spheres